HD 213885b: a transiting 1-d-period super-Earth with an Earth-like composition around a bright ($V = 7.9$) star unveiled by *TESS*

Néstor Espinoza [1,2]⋆†‡ Rafael Brahm,[3,4,5] Thomas Henning,[2] Andrés Jordán,[5,6,7]
Caroline Dorn,[8] Felipe Rojas,[4,6,7] Paula Sarkis,[2] Diana Kossakowski,[2]
Martin Schlecker,[2] Matías R. Díaz [9] James S. Jenkins [9] Claudia Aguilera-Gomez,[10]
Jon M. Jenkins,[11] Joseph D. Twicken,[12] Karen A. Collins,[13] Jack Lissauer,[11]
David J. Armstrong [14,15] Vardan Adibekyan,[16] David Barrado,[17] Susana C.
C. Barros,[16] Matthew Battley,[14,15] Daniel Bayliss [14,15] François Bouchy,[18]
Edward M. Bryant,[14,15] Benjamin F. Cooke,[14,15] Olivier D. S. Demangeon,[16]
Xavier Dumusque,[18] Pedro Figueira,[15,19] Helen Giles [18] Jorge Lillo-Box,[19]
Christophe Lovis,[18] Louise D. Nielsen [18] Francesco Pepe,[18] Don Pollacco,[14]
Nuno C. Santos,[16,20] Sergio G. Sousa [16] Stéphane Udry,[18] Peter J. Wheatley [14,15]
Oliver Turner [18] Maxime Marmier,[18] Damien Ségransan,[18] George Ricker,[21]
David Latham,[13] Sara Seager,[21] Joshua N. Winn,[22] John F. Kielkopf [23] Rhodes Hart,[24]
Geof Wingham,[25] Eric L. N. Jensen,[26] Krzysztof G. Hełminiak [27] A. Tokovinin [28]
C. Briceño,[29] Carl Ziegler,[29] Nicholas M. Law,[30] Andrew W. Mann,[30] Tansu Daylan,[20]§
John P. Doty,[31] Natalia Guerrero,[20] Patricia Boyd,[32] Ian Crossfield,[21]
Robert L. Morris,[11,12] Christopher E. Henze[11] and Aaron Dean Chacon[11,33]

Affiliations are listed at the end of the paper

ABSTRACT
We report the discovery of the 1.008-d, ultrashort period (USP) super-Earth HD 213885b (TOI-141b) orbiting the bright ($V = 7.9$) star HD 213885 (TOI-141, TIC 403224672), detected using photometry from the recently launched *TESS* mission. Using FEROS, HARPS, and CORALIE radial velocities, we measure a precise mass of $8.8 \pm 0.6\,\mathrm{M_\oplus}$ for this $1.74 \pm 0.05\,\mathrm{R_\oplus}$ exoplanet, which provides enough information to constrain its bulk composition – similar to Earth's but enriched in iron. The radius, mass, and stellar irradiation of HD 213885b are, given our data, very similar to 55 Cancri e, making this exoplanet a good target to perform comparative exoplanetology of short period, highly irradiated super-Earths. Our precise radial velocities reveal an additional 4.78-d signal which we interpret as arising from a second, non-transiting planet in the system, HD 213885c, whose minimum mass of $19.9 \pm 1.4\,\mathrm{M_\oplus}$ makes it consistent with being a Neptune-mass exoplanet. The HD 213885 system is very interesting from the perspective of future atmospheric characterization, being the second brightest star to host an USP transiting super-Earth (with the brightest star being, in fact, 55 Cancri). Prospects for characterization with present and future observatories are discussed.

⋆ E-mail: nespinoza@stsci.edu
† Bernoulli Fellow.
‡ IAU-Gruber Fellow.
§ Kavli Fellow.

1 INTRODUCTION

The successfully launched and currently operating *Transiting Exoplanet Survey Satellite* (*TESS*; Ricker et al. 2015) is set to become one of the most important missions in the search for small, characterizable rocky exoplanets. Currently exploring almost the whole sky on the hunt for transiting exoplanets orbiting bright (V < 13) stellar hosts, *TESS*' primary mission is to generate a sample of small (<4 $R_\oplus$) exoplanets for which precise masses and even atmospheric characterization will be possible, revolutionizing our view of these small, distant worlds.

Among the distinct populations of small exoplanets, one of the most interesting is the so-called ultrashort period (USP) exoplanets. These are planets that orbit at extremely short periods ($P \leq 1$ d), smaller than about 2 $R_\oplus$, and which appear to have compositions similar to that of the Earth (Winn, Sanchis-Ojeda & Rappaport 2018). Although almost a hundred of these systems have been found by the *Kepler* mission, with which it was found that these exoplanets are extremely rare (about as rare as hot jupiters, Sanchis-Ojeda et al. 2014), only a handful of them have precise radii and masses, as the stars in the *Kepler* field are typically much too faint for spectroscopic follow-up. Transit surveys like *TESS*, however, are the perfect haystacks to find these rare needles as they are designed to find short-period transiting exoplanets around bright stellar hosts, allowing us to explore the yet poorly understood dimension of mass and, thus, bulk composition of these interesting extrasolar worlds. In addition, missions like *TESS* are extremely important for exoplanets such as USPs as they will generate a sample of them which will be prime targets for future atmospheric follow-up with missions like the upcoming *James Webb Space Telescope* (*JWST*), which will in turn allow us to explore the exciting dimension of atmospheric composition of these small, short-period exoplanets (see e.g. the case of 55 Cancri e; Demory et al. 2016; Angelo & Hu 2017; Miguel 2019).

The possibility to perform spectroscopic follow-up for these USPs is in turn also interesting because of another fact: the inclination between the orbits of multiplanetary systems appears to be larger for short-period exoplanets in tight orbits ($\Delta i = 6.7 \pm 0.6$ deg for planets with $a/R_* \leq 5$ versus 2.0 ± 0.1 for planets with $5 < a/R_* < 12$, Dai; Masuda & Winn 2018), which might be a signature of orbital migration due to excitation effects such as high-eccentricity migration (Petrovich, Deibert & Wu 2019). If this effect is indeed the one dominating in systems having USPs, then detecting transits of more than one planet in multiplanetary systems might be intrinsically harder to do than for systems not having them, as the increased mutual inclination between the exoplanets in the system might prevent us from observing the transits of the other members of it. However, if their inclinations are within the same order of magnitude, these extra members might be found via high-precision spectroscopic follow-up, and this might in turn provide valuable constraints on the mutual inclinations between the exoplanets of these systems that might aid in the understanding of the formation of these rare, small exoplanets.

In this work, we present the discovery and characterization of a new USP discovered by the *TESS* mission, HD 213885b (TOI-141b), characterized due to precise radial-velocity measurements from FEROS, HARPS, and CORALIE. In addition to the tight constraint on the mass of this new exoplanet, our radial-velocity measurements reveal the presence of an additional non-transiting exoplanet in the system, HD 213885c (TOI-141c).

We organize this work as follows. In Section 2, we present the data used to make the discovery of this multiplanet system. In Section 3, we present the analysis of this data, in which we derive the properties of both the star and the planets in the system. In Section 4, we present a discussion on the system and the implication of this discovery to both the overall population of small exoplanets and the known USPs and in Section 5, we present the conclusions of our work.

2 DATA

2.1 *TESS* photometry

TESS photometry for TOI-141 was obtained in short-cadence (2-min) integrations from 2018 July to August (during a total time span of 27.9 d) in *TESS* Sector 1 using Camera 2. The *TESS* Science Processing Operations Center (SPOC) photometry was retrieved from the alerts webpage,[1] which provide either simple aperture photometry (SAP_FLUX) or the systematics-corrected photometry (PDCSAP_FLUX), a procedure performed by an adaptation of the Kepler Presearch Data Conditioning algorithm (PDC; Smith et al. 2012; Stumpe et al. 2012; Stumpe et al. 2014) to *TESS*. We use this latter photometry along with its provided errorbars (PDCSAP_FLUX_ERR) in the rest of this work; we refer to this photometry as the PDC photometry in what follows. Both, the SAP and PDC median-normalized photometry provided by the *TESS* alerts are presented in Fig. 1. For the analysis that follows, we remove two portions of the data: the portion (in BJD – 2457000) between 1347.5 and 1349.3, which was obtained during a period of increased spacecraft pointing jitter (see Huang et al. 2018), and the region after 1352, which shows an evident relatively short but significant decrease in flux which we found might give rise to biases in our analysis.

The *TESS* alerts diagnostics, generated using the tools outlined in Twicken et al. (2018), Jenkins et al. (2016), and Li et al. (2019) that have been adapted to work with *TESS* data, present this system as having a 1-d transit signal present in the data, which we refer to as TOI-141.01. The transit signature of this planet passes all the data validation (DV) tests (e.g. comparison of even and odd transits to screen against eclipsing binaries, ghost diagnostic tests to help rule out scattered light or background eclipsing binaries, among others) but the difference image centroiding test, likely due to the star being slightly saturated. From a difference image analysis done within the DV, however, the transit source is coincident with the core of the stellar point spread function (PSF), so it is clear the transit events happen on the target and not in, e.g. nearby bright stars. In order to confirm this signal and search for additional ones in the photometry, we ran the box least-squares algorithm (BLS; Kovács, Zucker & Mazeh 2002) on the data using a PYTHON implementation of this

---

[1] https://tess.mit.edu/alerts/
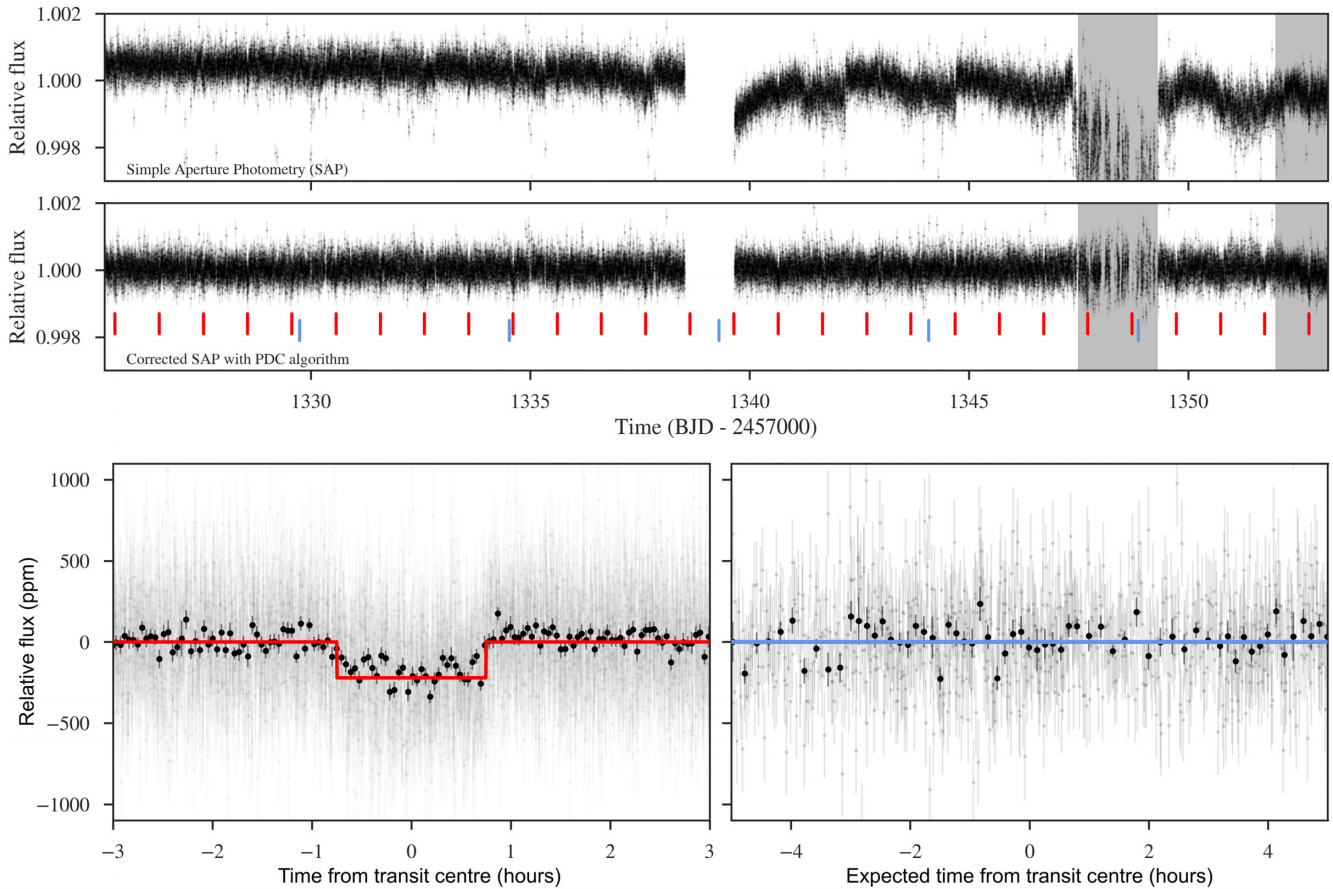
Figure 1. Top panels. *TESS* photometry for TOI-141. The upper panel shows the simple aperture photometry (SAP) provided by the *TESS* alerts (`SAP_FLUX`) along with the corresponding errors (`SAP_FLUX_ERR`) after normalizing for the median flux. The same photometry but systematics corrected via the PDC algorithm, also provided by the *TESS* alerts (`PDC_SAP_FLUX`) is shown in the bottom panel along with the corresponding errors (`PDC_SAP_FLUX_ERR`). Red lines indicate transits of the 1-d planetary candidate TOI-141.01 for which (200 ppm) transits can be easily observed by eye in the photometry. Blue lines indicate the expected position of transits of a second, 4.75-d sinusoidal signal found on the radial-velocity measurements (see Section 3.3) – no transits are evident at those times. Grey regions indicate portions of the time series left out of our analysis (see text). Bottom panels. Phased photometry at interesting periods. The leftmost phased photometry shows the photometry phased at the period of TOI-141.01 (grey points); black points show binned data points for visualization. Red line indicates the box model implied by our BLS search. The right-hand panel shows the same for the 4.75-d sinusoidal signal found in our radial-velocity measurements (see Section 3.3), where the reported time of transit centre is the expected time given our radial velocities. No transit is evident.

algorithm by Daniel Foreman-Mackey, `bls.py`.[2] Significances of the possible peaks were computed by running the algorithm on a mock data set, which contained the same median flux as the *TESS* photometry, and to which we added white-Gaussian noise whose standard deviation was defined as the provided errorbars at each time stamp. This procedure was ran 100 times, giving 100 BLS powers at each period, with which the mean BLS power and the corresponding standard deviation at each period was calculated. A peak in the BLS spectrum of the original data was then considered significant and was later inspected if it deviated by more than 5σ from this white-Gaussian noise spectrum. We ran the BLS on the search of transits with periods between 0.1 and 14 d (the latter chosen as around half the total time span of the *TESS* observations; 5000 periods were considered between those limits), searching for transits with durations between $q = 0.01$ and $q = 0.09$ in phase space.

Using the BLS on the PDC photometry, the largest peak in the BLS periodogram was located at around the same period as the

one reported on the *TESS* alerts, i.e. at 1.007 d, with a depth of around 200 ppm. The peak is highly significant – greater than 100 standard deviations above the mean BLS power at this period. It is interesting to note that the transits of this planetary candidate are individually visible in the light curve of TOI-141 presented in Fig. 1, indicated in that figure by red lines. We removed the in-transit points corresponding to TOI-141.01 and repeated the same procedure on the masked data. A couple of peaks emerge in the BLS periodogram just above our 5σ threshold, but when phasing the data at those periods, no evident transit signature emerges. In addition, those peaks are only at specific periods, and thus very narrow (one or two points) in the BLS periodogram. We thus conclude that no more significant transit-like signals are present in the BLS periodogram of our data. Possible additional signals in the photometry were also inspected using the Transiting Planet Search (TPS) within the SPOC DV component, which as mentioned above has been recently adapted to work with *TESS* data (Jenkins et al. 2016; Twicken et al. 2018; Li et al. 2019). No additional transiting planets were found with those tools either.

It is important to note that the aperture used to obtain the *TESS* photometry encompasses about 3 *TESS* pixels in radius around

[2]https://github.com/dfm/bls.py

the target, which amounts to an on-sky aperture of about 1 arcmin which in turn could lead to the light of other stars to contaminate the aperture. This could in turn give rise to possible dilutions of the observed transits, which could lead to misdetermination of the transit parameters, and to possible false-positives, which could led us to believe this is an exoplanetary system when in reality the observed *TESS* transit events could be due to a blend with a nearby eclipsing binary. In particular, the *TESS* aperture includes light not only from TOI-141 (which has a *TESS* magnitude of 7.358 ± 0.018), but also from five nearby stars: two faint stars, which we denote C1 and C2 in what follows, at about 30 arcsec from the target detected by both 2MASS (2MASS IDs: 22360031-5952070 and 22355219-5952034, for C1 and C2, respectively) and *Gaia* (Gaia Source IDs 6407428925971511808 and 6407428960331344512, for C1 and C2, respectively; Gaia Collaboration 2018), and three additional stars fainter than C1 and C2 by *Gaia* (Gaia Source IDs: 6407428891610548736, 6407428925970566272 and 6407434801486912768), the brightest of which has a *Gaia* magnitude of $G = 19.86$ – implying a $\Delta G = 12.1$ with TOI-141.

Assuming the magnitude difference in the *TESS* passband to be similar to the difference in the *Gaia* passband, the three faint stars detected by *Gaia* and not 2MASS are negligible sources of light in practice to the *TESS* aperture (if any of these were a totally eclipsing binary, for example, they would lead to transit depths of about 15 ppm; in terms of light-curve dilution, they amount to less than 0.0015 per cent of the light in the aperture). For C1 and C2, using the relations in Stassun et al. (2018), their *TESS* magnitudes are $T_{C1} = 16.862 \pm 0.025$ and $T_{C2} = 16.417 \pm 0.023$, respectively (calculated using the 2MASS J and *Gaia* G magnitudes of these stars, which are the magnitudes that have the smaller errorbars, and propagating the errors on the relations of Stassun et al. 2018 in quadrature to the photometric errors). This implies a magnitude difference with TOI-141 in the *TESS* passband of 9.504 ± 0.031 and 9.059 ± 0.029 for C1 and C2, respectively, thus amounting for 0.041 per cent of the light in the *TESS* aperture. If any of those stars were to produce the observed transits in the *TESS* photometry of TOI-141.01, they would have to be variable objects producing periodic 1-d dimmings of at least 80 per cent of their light. We explore this possibility with follow-up light curves in the next subsection.

2.2 Photometric follow-up

Photometric follow-up was performed as part of the *TESS* Follow-up Program (TFOP) SG1 Group. We used the `TESS Transit Finder`, which is a customized version of the TAPIR software package (Jensen 2013), to schedule photometric time series follow-up observations. Observations of TOI-141.01 were obtained on 2018 September 11, using the CDK700 27-inch telescope at Mount Kent Observatory (MKO). The observations were made in r' using 128 s 'deep' exposures, effectively saturating TOI-141 but gathering enough photons to provide precise photometry for the fainter companion stars in order to rule out false-positive scenarios. The observations covered around 3 h, and effectively covered the predicted ingress and egress events. We used ASTROIMAGEJ (Collins et al. 2017) to calibrate the data and extract the differential aperture photometry of the target and nearby stars. All stars within 2 arcmin turned out to have a constant brightness to within 10 per cent. Dimmings at the 80 per cent or larger for C1 and C2 can be confidently ruled out by these observations; however, C1 showed a 70 per cent *rise* in the photometry around the expected mid-transit time of TOI-141.01, which was due to an instrumental effect: due to
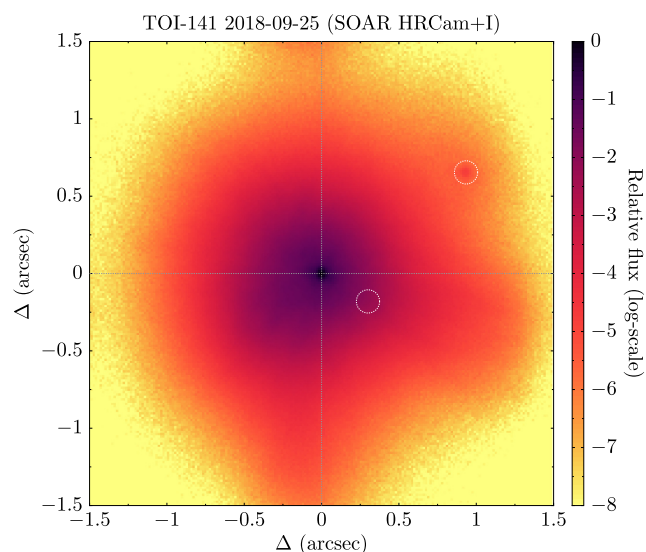
Figure 2. 'Lucky' image obtained with the HRCam at the 4.1-m SOAR telescope in the *I* band for TOI-141. The distant companion at 1.19 arcmin (indicated by a white circle in the figure) is evident from the image, whereas the closer 0.4 arcmin companion (also indicated) is not; this was detected via speckle ACF (see text).

the rotation of the field, some of the diffraction spikes of TOI-141 fell on the aperture used to extract the photometry of C1 at these times generating this increase in the relative flux of this object. It is important to stress here that although mid-transit was lost due to this effect, the light curve before this event showed no large variations as the ones expected from an eclipsing binary causing the *TESS* transits (the precise transit ephemerides for this system ensure we should have caught at least an ingress event if this was indeed an eclipsing binary).

The observations presented above thus rule out any possible near eclipsing binary as being responsible for the transit events observed in the *TESS* light curve.

2.3 Speckle imaging

Speckle imaging for TOI-141 was obtained on 2018 September 24, using the High-Resolution Camera (HRCam) at the 4.1-m Southern Astrophysical Research (SOAR) telescope located in Cerro Pachón, Chile, in the *I* band; the co-added images are presented in Fig. 2. The instrument and the corresponding analysis and reductions of data obtained with it is detailed in Tokovinin (2018). These observations, and the subsequent analysis of the autocorrelation function (ACF) of the image, which provides better dynamic range than working on the images directly (see Tokovinin 2018, for details), reveal two companions to TOI-141: one at a separation of 1.19 arcmin from TOI-141 at an angle of 305 deg, and another at a separation of 0.4 arcmin from the target at 239 deg, with magnitude differences of $\Delta I = 5.4$ and $\Delta I = 4.9$, respectively. As will be shown in Section 3, given the observed radial-velocity variations in phase with the transit ephemerides observed by *TESS* – and given these companion stars are too faint to produce any measurable signal in our radial-velocity measurements – it is very unlikely the companion stars revealed by these speckle imaging observations are the ones producing the transit events. These stars, however, could be important to constrain the possible transit dilutions they imply for our target. However, given these objects are not detected

Table 1. Radial-velocity measurements obtained for TOI-141.

Time (BJD)	Radial-velocity (m s^{-1})	Error (m s^{-1})	Exposure time (s)	Instrument
2458409.7085776	36164.16	0.56	900	HARPS
2458412.4991098	36146.57	0.39	900	HARPS
2458412.5935471	36149.97	0.46	900	HARPS
2458412.6969091	36153.13	0.55	900	HARPS
⋮	⋮	⋮	⋮	

Note. This table will be available in machine-readable form in the online journal. A portion is shown here for guidance regarding its form and content.

in *Gaia* DR2 (Gaia Collaboration 2018), and that only one-band observations are available, we cannot calculate either if they are physically bound nor their predicted *TESS* magnitudes in order to calculate the dilution these stars would imply in the *TESS* bandpass. If we assume the delta magnitudes in *I* band are similar to the *TESS* magnitudes, then these stars would account for about 1.8 per cent of the total flux in the *TESS* aperture. For a 200 ppm transit depth as the one detected by the *TESS* photometry for TOI-141.01, this would imply a dilution of about the same per cent of this transit depth (i.e. a depth about 4 ppm smaller) – this is well below the error on the transit depth, which as it will be shown in Section 3, is of the order of 12 ppm.

It is important to notice that, because TOI-141 is a relatively close system (48 pc – see Section 3), monitoring the system via high angular resolution in the future (e.g. a few years) might reveal if these companions detected with our observations are physically associated or not with TOI-141. We encourage future observations in order to determine if this is the case.

2.4 FEROS radial velocities

High-precision radial velocities were obtained for TOI-141 with the Fiber-fed Extended Range Optical Spectrograph (FEROS; Kaufer & Pasquini 1998) mounted at the 2.2-m MPG telescope at La Silla Observatory between 2018 September and October by the Chile-MPIA group. A total of 175 radial-velocities (RV) measurements were obtained with a simultaneous ThAr calibration using 200 s exposures. The RVs were extracted from the spectra using the customized CERES pipeline (Brahm, Jordán & Espinoza 2017a), which performs all the process of extraction from basic bias, dark and flat-field corrections (including scattered light) to order tracing, wavelength calibration, and cross-correlation matching of the spectrum with templates to obtain the RVs from the spectra. Although based on standard stars the precision that the CERES pipeline obtains with FEROS is 7 m s^{-1}, we found that with some modifications to the standard acquisition of FEROS frames one can achieve 3 m s^{-1} precision for $V = 8$ stars: simply by turning the ThAr lamp around 20 min before it is used, and taking a long series of ThAr calibration images to select the best one as reference greatly improves the precision one can achieve with FEROS using CERES. We followed these procedures for the obtention of the RVs of TOI-141 and imposed this 3 m s^{-1} noise floor to the star based on the monitoring of standard stars.

The FEROS observations showed radial velocities in phase with the transit ephemerides of TOI-141.01, showing an amplitude of about 5 m s^{-1}. In addition, they also showed an evident extra sinusoidal variation at a period of about 4.78 d. These signals will be analysed in detail in Section 3. The data are presented in Table 1.

2.5 HARPS radial velocities

High-precision radial velocities were also obtained with the High Accuracy Radial velocity Planet Searcher (HARPS) mounted at the ESO La Silla 3.6-m telescope (Mayor et al. 2003). These data were obtained by three groups: the Chile-MPIA group (14 measurements in 2018 September), the NCORES group (14 measurements in 2018 October), and the U. de Chile group (19 measurements between 2018 October and November), all of which were obtained using simultaneous ThAr calibration lamps. In total, 47 measurements were obtained for TOI-141 between 2018 September and November. The conditions during the 2018 September run were suboptimal, which in turn led us to use longer exposure times on those nights of 900 s. Conditions were photometric for the rest of the observing runs, and so 300 s exposures were used in those nights to gather spectroscopic measurements for TOI-141. The radial velocities were obtained with both the CERES pipeline (Brahm et al. 2017a) and the HARPS DRS pipeline. Although both gave consistent results, the CERES pipeline results have much larger long-term errors as monitored by standard stars than the quoted attainable precision by the DRS pipeline. Because of this, we decided to use the DRS instead of the CERES results in this work. The RV precision of those data points varied with the exposure times – 0.5 m s^{-1} for 900 s exposures and 2 m s^{-1} for 300 s exposures. The data are presented in Table 1.

2.6 CORALIE radial velocities

Additional data were obtained with the CORALIE instrument, mounted on the 1.2-m Euler Telescope at the La Silla Observatory (Queloz et al. 2001) both prior to the *TESS* observations and after the *TESS* observations. A first set of data, here denoted CORALIE07, were taken between 2008 August and 2013 October (seven radial-velocity measurements) and a second set of data, here denoted CORALIE14, were taken between 2016 August and 2018 September (eight radial-velocity measurements). From this latter set, six data points were taken after the *TESS* alerts were released. These data points have precisions between 3 and 4 m s^{-1}, and the radial velocities were analysed with the official CORALIE pipeline. Two extra data points to the just mentioned ones were obtained in 1990 July and 1994 August by CORAVEL (Baranne, Mayor & Poncet 1979), and another set of 12 radial-velocity data points were taken between 2001 September and 2006 September with CORALIE; however, we do not use those measurements in this work as they show errors in excess of the precision needed to constrain the masses of the exoplanets presented in this work. In total, thus, in this work we use 15 radial-velocity measurements from CORALIE.

It is important to note here that the CORALIE instrument was upgraded in 2014 November (see e.g. Maxted et al. 2016). This means that the zero-point offset between the CORALIE07 and

CORALIE14 radial velocities is different. Because of this reason, here we treat each as an independent data set, meaning that in the analysis to be described in Section 3.3, we consider different systemic velocities and jitters for each of those data sets. The data are presented in Table 1.

3 ANALYSIS

3.1 Stellar properties

We followed the iterative procedure described in Brahm et al. (2018a, b) to determine the physical parameters of TOI-141. First, we used the co-added HARPS spectra to compute the atmospheric parameters of TOI-141 by using the ZASPE code (Brahm et al. 2017b), which compares the observed spectrum with synthetic ones in the spectral regions that are most sensitive to changes in the atmospheric parameters. Then we combined the *Gaia* DR2 parallax and the available photometry to compute the stellar radius and extinction using an MCMC code.[3] Finally, we determined the stellar mass and age by searching for the Yonsei–Yale evolutionary model (Yi et al. 2001) that matched the observed stellar radius and spectroscopic effective temperature through another MCMC code.[4] With the derived stellar mass and radius, we computed a new value for the $\log(g)$ which is held fixed in a new ZASPE iteration, followed by the same steps that were just described. The final stellar parameters obtained for TOI-141 are presented in Table 2.

3.2 Stellar abundances

Stellar abundances are important to constrain possible interior composition models of exoplanets orbiting host stars, as they can give prior information to be used by structure modelling in order to constrain the composition of an exoplanet (see Section 4.2). Because of this, we extracted abundances from the HARPS (co-added) spectra of important refractory and volatile elements that could aid as priors in such an analysis. We use a standard LTE analysis with the 2017 version of MOOG (Sneden 1973) and Kurucz ATLAS9 model atmospheres (Castelli & Kurucz 2003), measuring the equivalent widths of Si, Ni, Mg, and C lines. The C abundance is based on two unblended lines at 5052.2 and 5380.3 Å with atomic parameters from Delgado Mena et al. (2010). For Si, Ni, and Mg, the line list of Neves et al. (2009) is used instead. We found abundances $A(X) = \log_{10} N(X)/N(H) + 12$, where $N(X)/N(H)$ is the atomic ratio between element X and hydrogen (H), where $N(H)$ is normalized to 10^{12} hydrogen atoms (i.e. $N(H) = 12$) for Si, Ni, Mg, and C – those are presented in Table 2. The errors reported consider the line-by-line scatter added in quadrature with errors produced by uncertainties on stellar parameters T_{eff}, [Fe/H], and $\log g_*$.

3.3 Joint analysis

The joint analysis of the photometry and radial velocities is performed here using a new code introduced in Espinoza, Kossakowski & Brahm (2019), JULIET, which is available via GitHub.[5] For our analysis in this work, JULIET uses BATMAN (Kreidberg 2015) to model the transit light curves and RADVEL (Fulton et al.

[3] https://github.com/rabrahm/rstar
[4] https://github.com/rabrahm/isoAR
[5] https://github.com/nespinoza/juliet

Table 2. Stellar parameters of TOI-141.

Parameter	Value	Source
Identifying information		
TIC ID	403224672	TIC
Gaia ID	6407428994690988928	*Gaia* DR2
2MASS ID	22355630–5951522	2MASS
RA (J2015.5, h:m:s)	$22^h35^m56.09$	*Gaia* DR2
Dec. (J2015.5, d:m:s)	$-59°51'53''.38$	*Gaia* DR2
Spectroscopic properties		
T_{eff} (K)	5978 ± 50	ZASPE
Spectral type	G	ZASPE
[Fe/H] (dex)	-0.04 ± 0.03	ZASPE
$\log g_*$ (cgs)	$4.3827^{+0.0095}_{-0.0097}$	ZASPE
$v\sin(i_*)$ (km s^{-1})	3.0 ± 0.2	ZASPE
$A(Si)$ (dex)	7.48 ± 0.09	MOOG
$A(Ni)$ (dex)	6.19 ± 0.11	MOOG
$A(Mg)$ (dex)	7.51 ± 0.06	MOOG
$A(C)$ (dex)	8.31 ± 0.13	MOOG
Photometric properties		
T (mag)	7.358 ± 0.018	*TESS*
B (mag)	8.4720 ± 0.0020	APASS
V (mag)	7.9960 ± 0.0020	APASS
r' (mag)	7.8500 ± 0.0010	APASS
i' (mag)	7.7130 ± 0.0020	APASS
z' (mag)	7.4690 ± 0.0020	APASS
J (mag)	6.806 ± 0.015	2MASS
H (mag)	6.501 ± 0.031	2MASS
Ks (mag)	6.419 ± 0.019	2MASS
Derived properties		
M_* ($M_\odot$)	$1.068^{+0.020}_{-0.018}$	YY[a]
R_* ($R_\odot$)	$1.1011^{+0.0080}_{-0.0075}$	*Gaia* DR2[a]
L_* ($L_\odot$)	$1.376^{+0.045}_{-0.049}$	YY[a]
M_V	$4.462^{+0.044}_{-0.042}$	YY[a]
Age (Gyr)	$3.80^{+0.66}_{-0.79}$	YY[a]
Distance (pc)	47.97 ± 0.14	*Gaia* DR2 + YY[a]
ρ_* (kg m^{-3})	1127 ± 33	YY[a]

Note. Logarithms given in base 10.
[a] Using stellar parameters obtained from ZASPE.

2018) to model the radial velocities. JULIET allows for a variety of parametrizations, and in particular allows us to incorporate Gaussian Processes (GPs) via the GEORGE (Ambikasaran et al. 2016) and the CELERITE (Foreman-Mackey et al. 2017) packages, which are implemented within JULIET for modelling underlying systematic and/or astrophysical signals present either in the radial velocities, the photometry or both, and to easily incorporate those into our modelling scheme. One of the key features of JULIET is its ability to perform model comparison, as nested sampling algorithms are used to compute posterior samples and, in particular, model pieces of evidence, Z_i, for a model M_i given the data, $\mathcal{D}$, i.e. $Z_i = p(\mathcal{D}|M_i)$. In this work within JULIET, we make use of MULTINEST (Feroz, Hobson & Bridges 2009) via the PYMULTINEST wrapper (Buchner et al. 2014) to explore the parameter space and perform model evidence calculations. This evidence estimation in turn allows to compute the probability of the model given the data, $p(M_i|\mathcal{D}) = p(M_i)p(\mathcal{D}|M_i)$ given a prior probability for model M_i, $p(M_i)$. Here, unless otherwise stated, we assume all models are a priori equiprobable and thus compare model pieces of evidence directly between models as in this case the posterior odds are simply $p(M_i|\mathcal{D})/p(M_j|\mathcal{D}) = Z_i/Z_j$. For ease of comparison, we here compare models using the difference of the (natural) log-evidences, $\Delta\ln Z_{i,j} = \ln Z_i/Z_j$. We have taken care to repeat the

Table 3. Priors used in our joint analysis of the TOI-141 system using JULIET for the analysis of TOI-141b and TOI-141c. Our stellar density prior is the one derived in Section 3.1. Here $p = R_p/R_*$ and $b = (a/R_*)\cos(i_p)$, where R_p is the planetary radius, R_* the stellar radius, a the semimajor axis of the orbit, and i_p the inclination of the planetary orbit with respect to the plane of the sky. e and ω are the eccentricity and argument of periastron of the orbits. $\mathcal{N}(\mu, \sigma^2)$ represents a normal distribution of mean μ and variance σ^2. $\mathcal{U}(a, b)$ represents a uniform distribution between a and b. $\mathcal{J}(a, b)$ represents a Jeffrey's prior (i.e. a log-uniform distribution) between a and b.

Parameter name	Prior	Units	Description
Parameters for TOI-141			
ρ_*	$\mathcal{N}(1127, 33^2)$	kg m^{-3}	Stellar density of TOI-141
Parameters for TOI-141b			
P_b	$\mathcal{N}(1.0079, 0.0100^2)$	d	Period of TOI-141b
$t_{0,b}$	$\mathcal{N}(2458379.9647, 0.0100^2)$	d	Time of transit centre for TOI-141b
$r_{1,b}$	$\mathcal{U}(0, 1)$	–	Parametrization[a] of Espinoza (2018) for p and b for TOI-141b
$r_{2,b}$	$\mathcal{U}(0, 1)$	–	Parametrization[a] of Espinoza (2018) for p and b for TOI-141b
K_b	$\mathcal{U}(0, 100)$	m s^{-1}	Radial-velocity semi-amplitude for TOI-141b
$\mathcal{S}_{1,b} = \sqrt{e_b} \sin \omega_b$	$\mathcal{U}(-1, 1)$	–	Parametrization[b] for e and ω for TOI-141b
$\mathcal{S}_{2,b} = \sqrt{e_b} \cos \omega_b$	$\mathcal{U}(-1, 1)$	–	Parametrization[b] for e and ω for TOI-141b
Parameters for TOI-141c			
P_c	$\mathcal{N}(4.75, 1.00^2)$	d	Period of TOI-141c
$t_{0,c}$	$\mathcal{N}(2458397.00, 1.00^2)$	d	Time of transit centre for TOI-141c
K_c	$\mathcal{U}(0, 100)$	m s^{-1}	Radial-velocity semi-amplitude for TOI-141c
$\mathcal{S}_{1,c} = \sqrt{e_c} \sin \omega_c$	$\mathcal{U}(-1, 1)$	–	Parametrization[b] for e and ω TOI-141c
$\mathcal{S}_{2,c} = \sqrt{e_c} \cos \omega_c$	$\mathcal{U}(-1, 1)$	–	Parametrization[b] for e and ω TOI-141c
Parameters for *TESS* photometry			
D_{TESS}	1 (fixed)	–	Dilution factor for *TESS*
M_{TESS}	$\mathcal{N}(0, 0.1^2)$	Relative flux	Relative flux offset for *TESS*
$\sigma_{w,TESS}$	$\mathcal{J}(0.1, 5000^2)$	Relative flux (ppm)	Extra jitter term for *TESS* light curve
$q_{1,TESS}$	$\mathcal{U}(0, 1)$	–	Quadratic limb-darkening parametrization[c] (Kipping 2013)
$q_{2,TESS}$	$\mathcal{U}(0, 1)$	–	Quadratic limb-darkening parametrization[c] (Kipping 2013)
RV parameters			
μ_{FEROS}	$\mathcal{N}(36140, 30^2)$	m s^{-1}	Systemic velocity for FEROS
$\sigma_{w,FEROS}$	$\mathcal{J}(0.01, 30^2)$	m s^{-1}	Extra jitter term for FEROS
μ_{HARPS}	$\mathcal{N}(36162, 30^2)$	m s^{-1}	Systemic velocity for HARPS
$\sigma_{w,HARPS}$	$\mathcal{J}(0.01, 30^2)$	m s^{-1}	Extra jitter term for HARPS
$\mu_{CORALIE07}$	$\mathcal{N}(36088, 30^2)$	m s^{-1}	Systemic velocity for CORALIE07[d]
$\sigma_{w,CORALIE07}$	$\mathcal{J}(0.01, 30^2)$	m s^{-1}	Extra jitter term for CORALIE07[d]
$\mu_{CORALIE14}$	$\mathcal{N}(36135, 30^2)$	m s^{-1}	Systemic velocity for CORALIE14[d]
$\sigma_{w,CORALIE14}$	$\mathcal{J}(0.01, 30^2)$	m s^{-1}	Extra jitter term for CORALIE14[d]

[a]To perform the transformation between the (r_1, r_2) plane and the (b, p) plane, we performed the transformations outlined in Espinoza (2018), which depend on r_1 and r_2, and a set of limits for the minimum and maximum p, p_l, and p_u, to consider: if $r_1 > A_r = (p_u - p_l)/(2 + p_l + p_u)$, then $(b, p) = ([1 + p_l][1 + (r_1 - 1)/(1 - A_r)], (1 - r_2)p_l + r_2 p_u)$. If $r_1 \leq A_r$, then $(b, p) = ([1 + p_l] + \sqrt{r_1/A_r} r_2 (p_u - p_l), p_u + (p_l - p_u)\sqrt{r_1/A_r}[1 - r_2])$. In this work, we set $p_l = 0$ and $p_u = 1$.
[b]We ensure in each sampling iteration that $e = \mathcal{S}_1^2 + \mathcal{S}_2^2 \leq 1$.
[c]To transform from the (q_1, q_2) plane to the plane of the quadratic limb-darkening coefficients, (u_1, u_2), we use the transformations outlined in Kipping (2013) for this law $u_1 = 2\sqrt{q_1} q_2$ and $u_2 = \sqrt{q_1}(1 - 2q_2)$.
[d]CORALIE07 corresponds to data taken between the 2007 and 2014 upgrade and CORALIE14 corresponds to data taken after the 2014 upgrade (see Section 2.6).

model evidence calculations several times in order to account for the miscalculation of errors on pieces of evidence known to happen in nested sampling algorithms (see Nelson et al. 2018); however, we note that in our case, given the large amount of data (especially given we have strong constraints on the ephemerides of at least one planet in this work from transit photometry), the empirically determined errors on the pieces of evidence (calculated by running each model run five times) are always $\ln Z < 1$ – typically of the order of 0.1.

3.3.1 Photometry-only analysis

For the analysis of the TOI-141 system, we first performed a photometry-only analysis with JULIET in order to find constraints on the time of transit centre and period of the orbit of TOI-141.01 using the priors defined for the photometric elements in Table 3, which were based on our BLS search and the *TESS* alerts best period for this candidate. We consider the possibility that the *TESS* photometry might need a GP to account for any residual time-correlated noise in the light curve, and for this we fitted both a transit model plus an exponential-squared GP and a transit model assuming a white-noise model only. We found that both models were indistinguishable from one another based on their model pieces of evidence ($\Delta \ln Z < 1$), and thus decided to use the simpler model (i.e. a no-GP, white-noise model) when analysing the PDC photometry. We note that for the white-noise model we add an extra photometric jitter term in quadrature to the reported uncertainties in order to account for miscalculations of the photometric uncer-

tainties or any residual astrophysical signal not captured by our modelling.

In addition to this fit, we also tried a fit assuming there is an additional transiting planet in the system to TOI-141.01, with the same photometric priors as the ones used for this candidate presented in Table 3, except for the period and time of transit centre; the first was left to freely vary between 0.1 and 14 d (for the same reason this were the trial periods in our BLS analysis in Section 2), whereas the second was left to vary from the time of the start of the observations to 15 d later. We found no evidence on the data for additional transiting planets ($\ln Z > 100$ in favour of the one-planet model) in agreement with our results from the BLS search in Section 2.

3.3.2 RV-only analysis

We ran a JULIET run on the radial velocities independently in order to see if we were able to find evidence for planets in the radial-velocity data set alone. For this, we ran three models: (1) no planet (i.e. variation in the data solely explained by the jitters of the data, which were let to float as free parameters), (2) one planet in the RVs, (3) two planets in the RVs. We modelled the planetary signals using simple Keplerians assuming circular orbits with the same priors as the radial-velocity elements in Table 3. However, for this exercise we gave wide log-uniform priors for the period from 0.1 to 30 d for both planets (with the constraint that one planetary period is always larger than the other in order to avoid multiple modes for exchangeable periods) and the times of transit centre set with uniform priors between the start of the observations and 30 d later.[6] The limit of 30 d was set as our most constraining RV data sets (the FEROS and HARPS data sets) are only ∼60 d in total duration, and as such periods up to half this baseline are reasonable to search in the data set.

The resulting pieces of evidence for the models strongly favour the one and two-planet models in the data over the no-planet model. The one-planet model converges to a posterior period of 4.75 ± 0.01 d, and it has a log-evidence 56 times larger than the no-planet model, i.e. the one-planet model is 24 orders of magnitude more likely than the null model. In turn, the two-planet model converges to both a period of 1.00940 ± 0.00036 d for one of the planets and of 4.7604 ± 0.0028 d for the other – this model in turn has a log-evidence 52 times larger than the one-planet model, and 108 times larger than the no-planet model. We note how in this two-planet model the smallest period is consistent with the period of the transit events observed by *TESS*, albeit with a small offset, most likely due to the sampling of the data (i.e. given a signal with a period equal to that of the transit ephemerides in our data, this offset is expected given the alias of 1 d the window function imprints on our radial-velocity measurements; see Dawson & Fabrycky 2010, for details, and our discussion below). This acts as an independent confirmation of the transit signal observed in the *TESS* photometry – we consider these observations thus confidently confirm the transit signatures observed by *TESS* as a bona fide exoplanetary signal, to which we refer to as TOI-141b in what follows.

The 4.8-d signal, although well fitted with a Keplerian, could also be caused by stellar activity and not by the reflex motion of

---

[6]In practice, this gave rise to many local minima corresponding to integer times the period along the observations but this is not a problem for the nested sampling algorithms used by JULIET – see Espinoza et al. (2018) for details on this point.

a planet around the star. We anticipate that this is not very likely, as the star's chromospheric emission as measured by the $\log R'_{\mathrm{HK}}$ has been actually measured before our observations to be quite low (-4.90 ± 0.05; Henry et al. 1996), which combined with its $B - V = 0.62$ colour, would imply it resides in the region where inactive stars reside in the $B - V$/$\log R'_{\mathrm{HK}}$ diagram. On top of this, assuming the stellar axis is aligned with the plane of the sky, we can derive a rotation period of the (equator of the) star of 18.58 ± 1.28 d from the stellar radius and the $v \sin i_*$ value presented in Table 2, which is much too large to explain the evident 4.8-d variations observed in our radial velocities. Indeed, the periodogram of monitored external variables, such as Mount Wilson's S-index shows no clear peak around the periods of interest, and the same results are obtained for the bisector span (Fig. 3). We none the less consider this possibility in the next subsection when we perform the joint photometric and RV analysis.

3.3.3 Photometric and RV analysis

With the above defined information, we performed a joint analysis of the photometry and radial velocity of TOI-141 using JULIET, which we use to jointly constrain all the parameters of the orbits of both TOI-141b and the possible 4.75-d planetary signal in the TOI-141 system. We use normal priors for the periods and time of transit centres of those signals, with mean values taken from our photometry and radial-velocity-only analyses, and with standard deviations enlarged by a factor of a thousand with respect to those found in those analyses. All the other parameters are left to explore the whole parameter space of physically plausible ranges.

In order to study the nature of the 4.8-d signal found in our radial-velocity-only analysis and any possible additional signals in the radial velocities, we performed two groups of joint analyses in which we explored (1) how strongly this extra signal is supported by the data, (2) what the nature of this extra signal is (i.e. planetary or stellar activity), and (3) if there is any evidence for additional signals on top of this extra signal in the radial velocities. To explore (1) and (2), we considered two possible models for this extra signal: a Keplerian or a GP. For the Keplerian model, we used the priors presented in Table 4. For the GP model, we used the same priors but instead of adding the parameters corresponding to planet c, we used a GP to account for the extra signal with three different possible kernels. The first was a squared-exponential kernel using either time, S-index, or bisector spans as inputs, i.e. a kernel of the form

$$k_{i,j}(\tau) = \sigma_{\mathrm{GP}}^2 \exp\left(-\alpha_{\mathrm{GP}}\tau^2\right),$$

where $\tau = x_i - x_j$, is the lag between the mentioned state variables (which were fed normalized – i.e. they were mean subtracted and divided by their standard deviations), σ_{GP} is the amplitude of this GP component, and α_{GP} is the inverse length-scale of this parameter. The second kernel we explored was the quasi-periodic kernel introduced by Foreman-Mackey et al. (2017), which is of the form

$$k_{i,j}(\tau) = \frac{B}{2+C} \mathrm{e}^{-\tau/L} \left[\cos\left(\frac{2\pi\tau}{P_{\mathrm{rot}}}\right) + (1+C)\right]$$

and where $\tau = t_i - t_j$ is the time lag. Here B and C are terms that normalize and amplify the kernel, whereas L is an exponential decay time-scale and P_{rot} is the period of the quasi-periodic GP. Finally, we also explored the widely used exp-sine-squared kernel
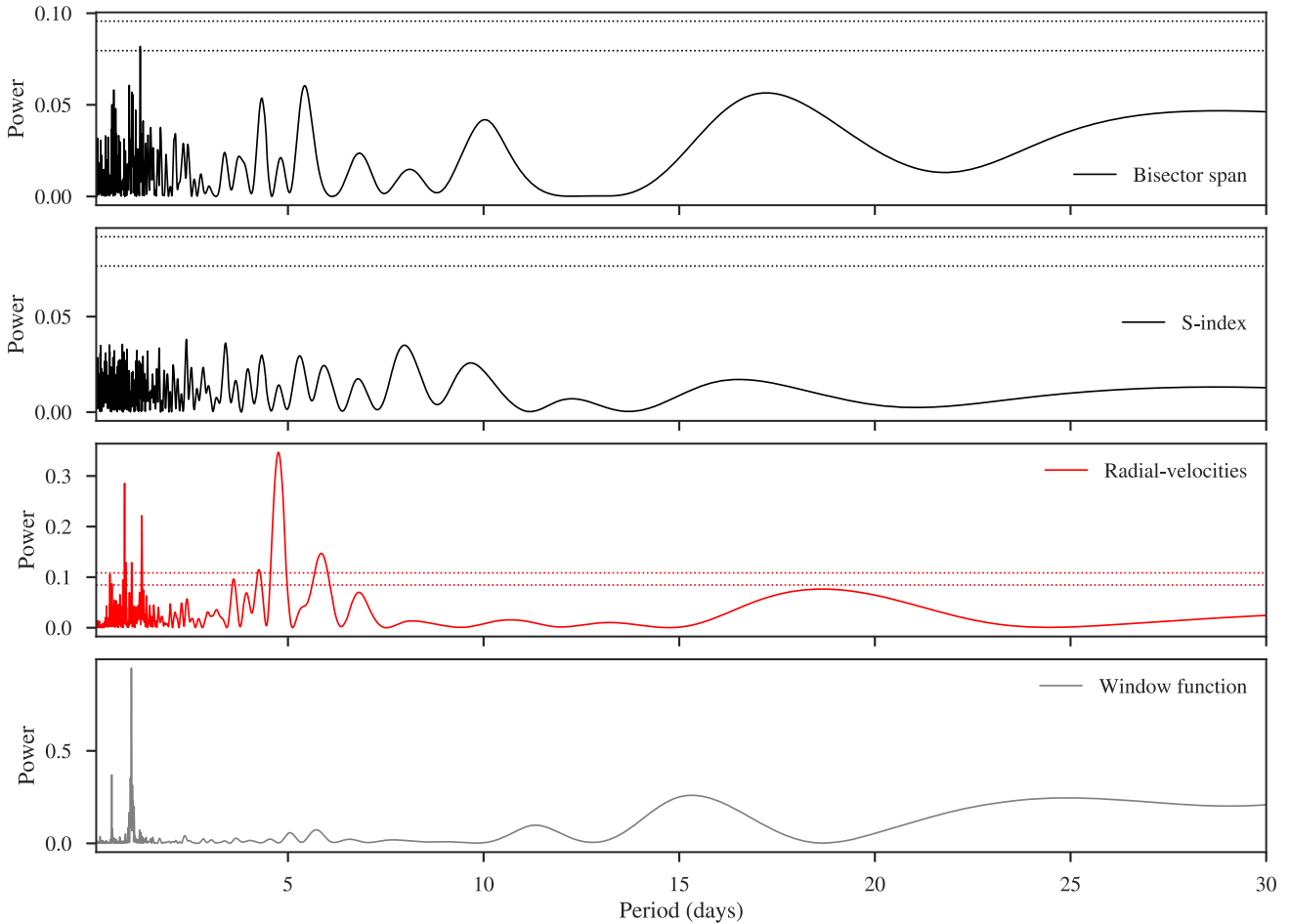
Figure 3. Generalized periodogram for the bisector span (top), S-index (second panel), the radial velocities (third panel), and the window function (bottom). Dotted lines in each panel denote the 1 per cent and 5 per cent false-alarm probabilities. Periodograms calculated with the Generalized Lomb–Scargle periodogram (Zechmeister & Kürster 2009) and with false-alarm probabilities calculated via bootstrapping with ASTROML (Vanderplas et al. 2012).

Table 4. Priors used for our fits including GPs. These were used in conjunction with the priors listed in Table 3.

Parameter name	Prior	Units	Description
Parameters for the squared exponential kernel			
$\sigma_{\rm GP}$	$\mathcal{J}(10^{-5}, 1000)$	m s^{-1}	Amplitude of GP component
$\alpha_{\rm GP}$	$\mathcal{J}(10^{-5}, 1000)$	–	Inverse length-scale of the GP component
Parameters for the quasi-periodic kernels			
$P_{\rm rot}$	$\mathcal{N}(4.75, 1.00^2)$	d	Period of the quasi-periodic component.
Parameters for (Foreman-Mackey et al. 2017) quasi-periodic kernel			
B	$\mathcal{J}(10^{-5}, 1000)$	m^2 s^{-2}	Amplitude of GP component
C	$\mathcal{J}(10^{-5}, 1000)$	–	Factor of GP component
L	$\mathcal{J}(10^{-5}, 1000)$	1 d	Length-scale of the quasi-periodic component
Parameters for the exp-sine-squared GP			
$\sigma_{\rm GP}$	$\mathcal{J}(10^{-5}, 1000)$	m s^{-1}	Amplitude of GP component
$\alpha_{\rm GP}$	$\mathcal{J}(10^{-5}, 1000)$	–	Inverse length-scale of the GP component
Γ	$\mathcal{J}(10^{-5}, 1000)$	–	Amplitude of the sine-squared term in the GP

of the form

$$k_{i,j}(\tau) = \sigma_{\rm GP}^2 \exp\left(-\alpha_{\rm GP}\tau^2 - \Gamma \sin^2\left[\frac{\pi\tau}{P_{\rm rot}}\right]\right),$$

where $\tau = t_i - t_j$ is again the time lag, $\sigma_{\rm GP}$ is the amplitude of the GP component, $\alpha_{\rm GP}$ is an inverse time-scale for the GP, Γ is the

amplitude of the periodic component of the GP, and $P_{\rm rot}$ is, again, the period of the quasi-periodic component. The priors used for the hyperparameters of those GP models are listed in Table 4.

The first four items in Table 5 show the results of this first group of fits performed on our data. As can be seen, among those models the best one given the data appears to be the one which

Table 5. Resulting log-evidences (and differences with respect to the model selected as the 'best' model – in bold) from different model fits to the full photometric and RV data sets with the priors defined in Tables 3 and 4 (see text). SE stands for results using a squared-exponential kernel, whereas FM stands for results using the Foreman-Mackey et al. (2017) quasi-periodic kernel. The value presented for the one planet + SE GP below corresponds to the model using time as a variable, which was the model that gave the best fit among that class of models. The two planet + SE GP model was selected as the best model as it is indistinguishable between the other two-planet GP fits ($|\Delta \ln Z < 1|$), and is the simpler (i.e. has lower number of free parameters) of them.

Model	$\ln Z$	$\Delta \ln Z$
Two planets	111 484.42	−49.0
One planet + SE GP	111 505.87	−27.5
One planet + exp-sine-squared QP GP	111 516.60	−16.8
One planet + FM QP GP	111 526.35	−7.07
Two planets + exp-sine-squared QP GP	111 533.07	−0.35
Two planets + SE GP	**111 533.42**	**0**
Two planets + FM QP GP	111 533.61	0.19

includes one planet (the transiting one) plus the kernel introduced by Foreman-Mackey et al. (2017). This result is interesting because the periodic component of the GP is clearly trying to fit for a 4.8-d periodic component plus some extra signal in the data in this case, which led us to believe that the best model could be one which has two Keplerians (one for the transiting planet and one for the 4.8-d signal) and an additional GP component on top of them (i.e. point 3 above). Motivated by this possibility, we performed a second group of fits with two Keplerians plus a GP, where we tried the same kernels as for the first group of fits (i.e. with the priors on the GP hyperparameters given in Table 4). The results of our fits for this second group of fits are also presented in Table 5 (three last items in the list).

As can be seen in Table 5, the models with the highest pieces of evidence are models with two planets and an additional GP component.[7] At face value, the model with the highest evidence is the one using the Foreman-Mackey et al. (2017) quasi-periodic kernel, but this model is in practice indistinguishable ($|\Delta \ln Z < 1|$) from both a fit using an exp-sine-squared kernel and a squared-exponential kernel. Interestingly, the quasi-periodic kernels in these two-planet fits actually provide no constraint on the extra residual periodic component – the posterior on the P_{rot} parameters only rules out periods smaller than about 5 d, and is uniform in the rest of the parameter space, which hints that the presence of any additional periodic signal (e.g. activity and/or extra planetary companions) is unlikely given our data. In fact, all three fits converge to the same posterior parameters for all the orbital and physical parameters of the planets in the system. Being the two-planet plus squared-exponential GP the simpler of the mentioned fits, we choose this as our best model in this case; this model is in turn superior to both the one-planet models assuming an extra squared-exponential kernel or a quasi-periodic kernel and to the two-planet fit without a GP component. Together with our discussion in the previous section that stellar activity indicators show no evident peaks in the
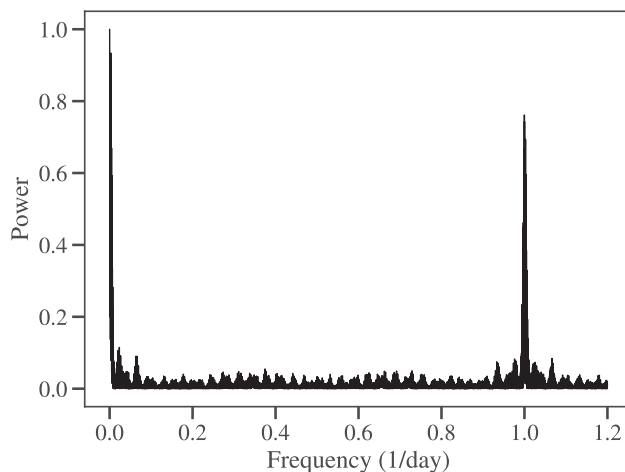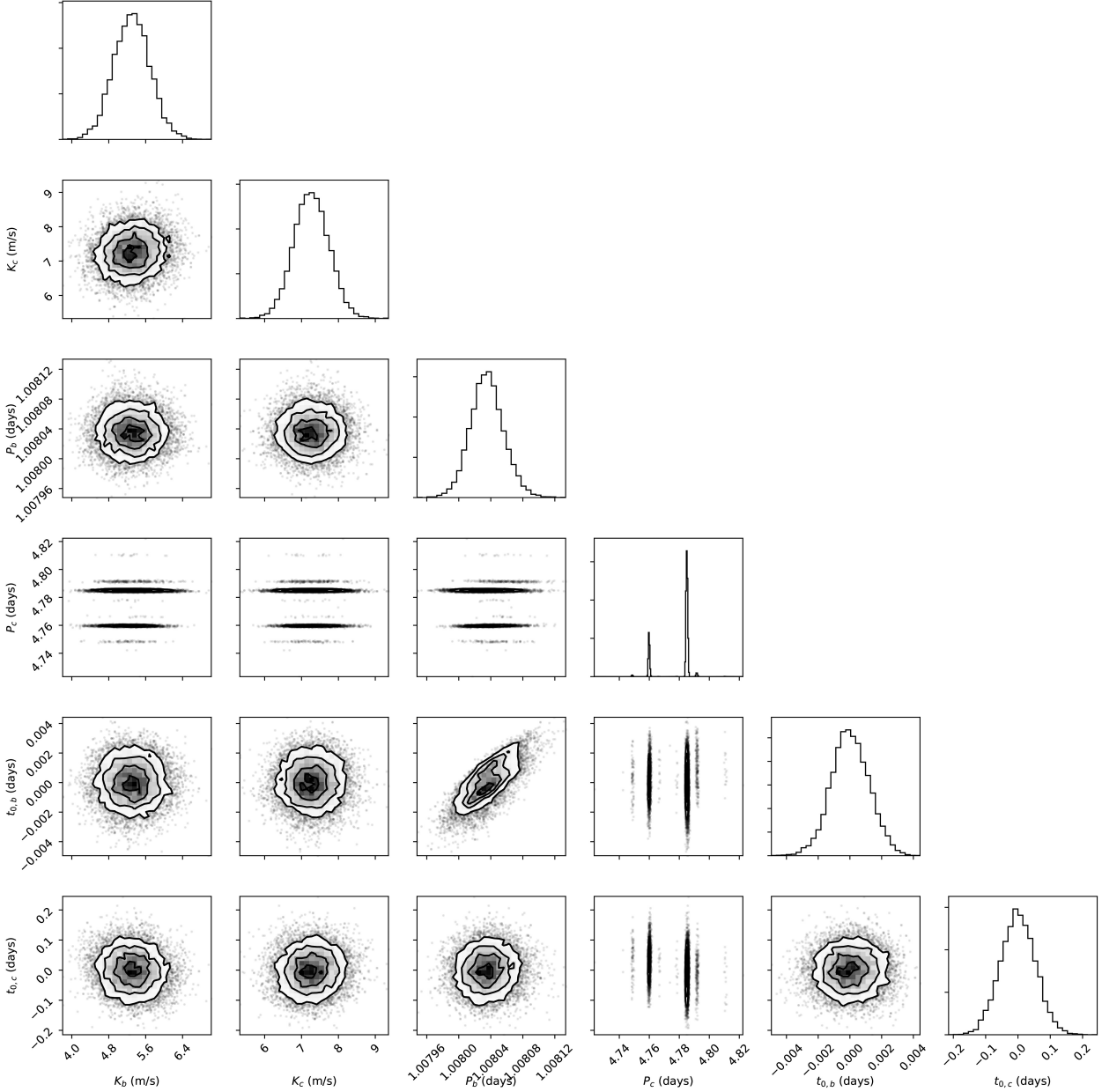

Figure 4. Window function of our radial-velocity samples. Two peaks emerge in the window shown here, one at $0.001 \, d^{-1}$ and another one at $1.00185 \, d^{-1}$.

periodogram at the periods of interest, and that the rotation period of the star is much longer than the period of interest, we take this as evidence that the observed signal is indeed caused by a non-transiting planet, to which we refer from now on to as TOI-141c. It is interesting to note that our posterior distribution for the period of planet TOI-141c is actually multimodal with the two main periods being at $4.759\,83^{+0.000\,46}_{-0.000\,43}$ and at $4.785\,03^{+0.000\,56}_{-0.000\,51}$ d. It is under this latter period that most of the posterior density is located, in fact. However, an additional piece of evidence that this latter one is the true period of TOI-141c comes from examining our window function (Fig. 4). The function shows the expected peak around the solar day ($1.0018 \, d^{-1}$ in our window function), which in turn is propagated also to lower and higher frequencies. In particular, the largest peak in our window function in frequency space is at $f_s = 0.001 \, d^{-1}$. Given a real frequency present in the data, thus, aliases of this frequency will emerge at $f_{alias} = f_{true} \pm mf_s$, where m is an integer, f_{true} is the true, underlying frequency embedded in the data set, f_{alias} is the generated alias, and f_s is a peak from the window function. Indeed, if the 4.785 03 period is the real period, then with $f_s = 0.001 \, d^{-1}$ this signal should generate aliasing signals at periods of 4.76 and 4.81 d, both of which we do see in our posterior distribution for the period. If the real period were 4.759 83 d, on the other hand, this should give rise to aliasing signals at periods of 4.78 and 4.73 d – the latter not being present in our posterior distribution. To make a quantitative assessment of this, we used the ALIASFINDER package (Stock & Kemmer, in preparation),[8] which implements the procedure for alias finding detailed in Dawson & Fabrycky (2010). Using this tool with both of these periods yields the same suggestion: that the 4.785 03 period is the real period, with the 4.759 83 period being an alias. Because of this, the period of $4.785\,03^{+0.000\,56}_{-0.000\,51}$ d is the one we report as our final estimate for the period of this exoplanet. We note that there is no strong correlation between the period and any other parameter in Fig. 5 – this multimodal nature, however, appears not only on our GP fits but also on our two-planet white-noise fits, which suggests that, indeed, these appear because of the sampling of the data. Importantly, this bimodal nature of this period, does not enlarge the uncertainties in the other retrieved parameters.

---

[7]We also tried three-planet fits, but these show much smaller log-evidences than the models presented here. A three-planet fit with the third component having a log-prior on the period from 5 to 100 gives a log-evidence worse than the best model presented in this work.

[8]https://github.com/JonasKemmer/AliasFinder

Figure 5. Corner plot of the posterior distribution of the main parameters of planet b and c, where the multimodality of the period of planet c is evident. The two main peaks of this multimodal distribution are located at $4.759\,83^{+0.000\,46}_{-0.000\,43}$ d and at $4.785\,03^{+0.000\,56}_{-0.000\,51}$ d. We note that for the time-of-transit centres, the plotted values are the median-subtracted values of the posteriors. This has been subtracted for clarity in the corner plot.

The posterior distribution of the parameters of our best-fitting model are presented in Table 6 for all the parameters except for the eccentricities and the jitter terms mentioned above – for those parameters we present upper limits based on the fits performed allowing those to vary freely in our JULIET runs; the corresponding posterior modelling of the data is presented in Fig. 6 for the photometry and Fig. 7 for the radial velocities. A close-up to the radial velocities showing how each component of our model adds to the full signal is presented in Fig. 8.

As can be observed in Fig. 8 and from the derived inverse length-scale reported in Table 6, the GP component tries to explain a stochastic variation with a typical time-scale $(1/\sqrt{2\alpha_{GP}})$ of $\sim$3 h with an amplitude of about $\sim$2 m s^{-1}. It is unlikely this is some kind of stellar oscillation, as the amplitude of them in radial velocities

of stars similar to the Sun like TOI-141 are about one order of magnitude smaller and occur at scales of minutes and not of hours (see e.g. Carrier & Bourban 2003; Elsworth & Thompson 2004). One possibility is that our GP component is modelling instrumental systematics; these could be coming mainly from the FEROS data set, which is the dominant source of RVs in our work, for which stability at the precision level attained in this work ($\sim$2 m s^{-1}) has not been tested so far at such time-scales.

The derived physical parameters presented in Table 6 for the transiting exoplanet TOI-141b present a remarkable similarity with the benchmark exoplanet 55 Cancri e (a.k.a. Janssen, Fischer et al. 2008; Winn et al. 2011). According to the latest analysis of this latter transiting exoplanet by Bourrier et al. (2018), 55 Cancri e has a radius of $R_p = 1.88 \pm 0.03\,R_\oplus$ and mass of $M_p = 8.0 \pm 0.3\,M_\oplus$,

Table 6. Posterior parameters obtained from our JULIET analysis for TOI-141b and TOI-141c.

Parameter name	Posterior estimate[a]
Posterior parameters for TOI-141b	
P_b (d)	$1.008\,035^{+0.000\,021}_{-0.000\,020}$
$t_{0,b}$ (BJD UTC)	$245\,8379.970\,43^{+0.0012}_{-0.0012}$
ρ_* (kg m^{-3})	$1127.4^{+31.8}_{-31.3}$
$r_{1,b}$	$0.783^{+0.022}_{-0.027}$
$r_{2,b}$	$0.014\,53^{+0.000\,41}_{-0.000\,42}$
K_b (m s^{-1})	$5.30^{+0.39}_{-0.39}$
e_b	0 (fixed[b], <0.24)
Posterior parameters for TOI-141c	
P_c (d)	$4.785\,03^{+0.000\,56}_{-0.000\,51}$
$t_{0,c}$ (BJD UTC)	$245\,8396.635^{+0.054}_{-0.054}$
K_c (m s^{-1})	$7.26^{+0.48}_{-0.47}$
e_c	0 (fixed[b], <0.16)
Posterior parameters for *TESS* photometry	
M_{TESS} (ppm)	$-21^{+2.2}_{-2.2}$
$\sigma_{w,TESS}$ (ppm)	$111.1^{+4.0}_{-4.0}$
$q_{1,TESS}$	$0.23^{+0.31}_{-0.17}$
$q_{2,TESS}$	$0.43^{+0.35}_{-0.29}$
Posterior RV parameters	
μ_{FEROS} (m s^{-1})	$361\,31.07^{+0.40}_{-0.40}$
$\sigma_{w,FEROS}$ (m s^{-1})	$0.88^{+0.82}_{-0.81}$
μ_{HARPS} (m s^{-1})	$361\,59.65^{+0.53}_{-0.53}$
$\sigma_{w,HARPS}$ (m s^{-1})	0 (fixed[b], <2.16)
$\mu_{CORALIE07}$ (m s^{-1})	$360\,88.8^{+1.8}_{-1.8}$
$\sigma_{w,CORALIE07}$ (m s^{-1})	0 (fixed[b], <8.68)
$\mu_{CORALIE14}$ (m s^{-1})	$361\,33.1^{+1.4}_{-1.5}$
$\sigma_{w,CORALIE14}$ (m s^{-1})	0 (fixed[b], <2.51)
σ_{GP} (m s^{-1})	$2.08^{+0.32}_{-0.29}$
α_{GP} (1 d^2)	$27.1^{+27.0}_{-17.2}$
Derived transit parameters for TOI-141b	
R_p/R_*	$0.014\,53^{+0.000\,41}_{-0.000\,42}$
$b = (a/R_*)\cos(i_p)$	$0.675^{+0.033}_{-0.041}$
a_b/R_*	$3.927^{+0.037}_{-0.037}$
i_p (deg)	$80.09^{+0.62}_{-0.50}$
u_1	$0.34^{+0.34}_{-0.23}$
u_2	$0.063^{+0.35}_{-0.27}$
Derived physical parameters for TOI-141b	
M_p (M$_\oplus$)	$8.83^{+0.66}_{-0.65}$
R_p (R$_\oplus$)	$1.745^{+0.051}_{-0.052}$
ρ_p (g cm^{-3})	$9.15^{+1.1}_{-1.0}$
g_p (m s^{-2})	$28.5^{+2.8}_{-2.7}$
a (au)	$0.020\,12^{+0.000\,15}_{-0.000\,12}$
T_{eq} (K)[c]	2128^{+13}_{-14}
Derived physical parameters for TOI-141c	
$M_p\sin(i_p)$ (M$_\oplus$)	$19.95^{+1.38}_{-1.36}$
a (au)	$0.056\,798^{+0.000\,44}_{-0.000\,32}$
T_{eq} (K)[c]	$1265.4^{+7.3}_{8.4}$

[a]Errorbars denote the 68 per cent posterior credibility intervals (CI).
[b]Limits denote the 95 per cent upper CI of fits allowing all orbits to be eccentric.
[c]Equilibrium temperatures calculated assuming 0 Bond Albedo.
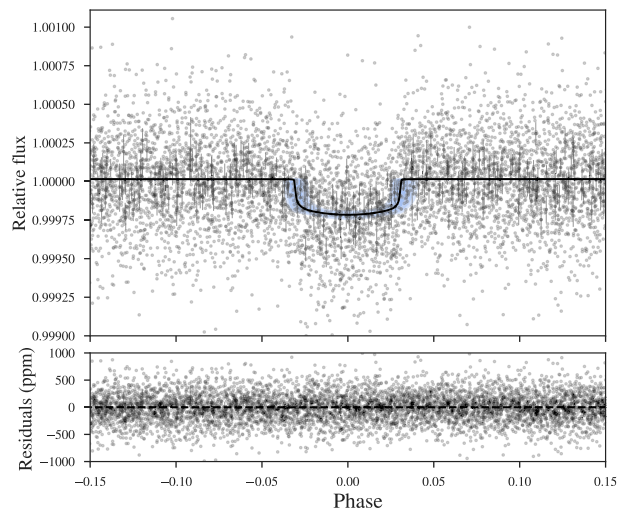
Figure 6. *Top. TESS* photometry phased around the period of TOI-141b (grey points; black points with errorbars correspond to 10-point binned photometry shown for illustration). The black line shows the median posterior model given the data, and blue bands denote its 68 per cent, 95 per cent, and 99 per cent posterior credibility bands. *Bottom.* Residuals obtained by subtracting the data with our median posterior model.

which implies a density of $\rho_p = 6.7 \pm 0.4$ g cm^{-3}. Similarly TOI-141b has a radius of $R_p = 1.745^{+0.051}_{-0.052}$ R$_\oplus$ and mass of $M_p = 8.83^{+0.66}_{-0.65}$ M$_\oplus$, which in turn implies a (larger, but still consistent at 2σ) density of $9.15^{+1.1}_{-1.0}$ g cm^{-3}. Both exoplanets, thus, have statistically indistinguishable masses and radii (TOI-141b is only $\Delta R_p = 0.135 \pm 0.06$ R$_\oplus$ smaller than 55 Cancri e, i.e. consistent with 0 within $\sim$2 standard deviations). In fact, this also applies to their irradiation levels as well: the zero-albedo equilibrium temperature of TOI-141b is only slightly higher than that of 55 Cancri e (only $\Delta T_{eq} \approx 200$ K hotter than 55 Cancri e). Thus, TOI-141b can be thought of as a very similar exoplanet to 55 Cancri e, making it almost an analogue in terms of the planetary properties, given the current data at hand. We discuss the prospects that TOI-141b provides for planetary characterization and comparative exoplanetology of transiting super-Earth exoplanets in light of this similarity in the next section.

The derived properties for TOI-141c are exciting as well. The minimum mass for TOI-141c of $M_p\sin(i_p) = 19.95^{+1.38}_{-1.36}$ M$_\oplus$ suggests a minimum mass of the order of that of Neptune. Given the transiting nature of TOI-141b, we thus expect the inclination of this exoplanet to be not much larger than its inner companion, implying a true mass of the same order as the one implied by its minimum mass in our analysis.

3.4 Searching for transits of TOI-141c

We used the *TESS* photometry to search for transits of TOI-141c. For this, we performed a JULIET run with the same priors as the ones defined in Table 3 for TOI-141c. We assumed a circular orbit for both exoplanets (as per our result in Section 3.3) and we added $r_{1,c}$ and $r_{2,c}$ as free parameters to TOI-141c with the same priors as the corresponding parameters for TOI-141b to allow a transiting scenario for TOI-141c. The resulting JULIET runs with and without a transiting TOI-141c with this parametrization significantly favoured the non-transiting model ($\ln Z = 5.4$ in favour of this model). Fig. 9 shows the posterior distribution of the impact parameter
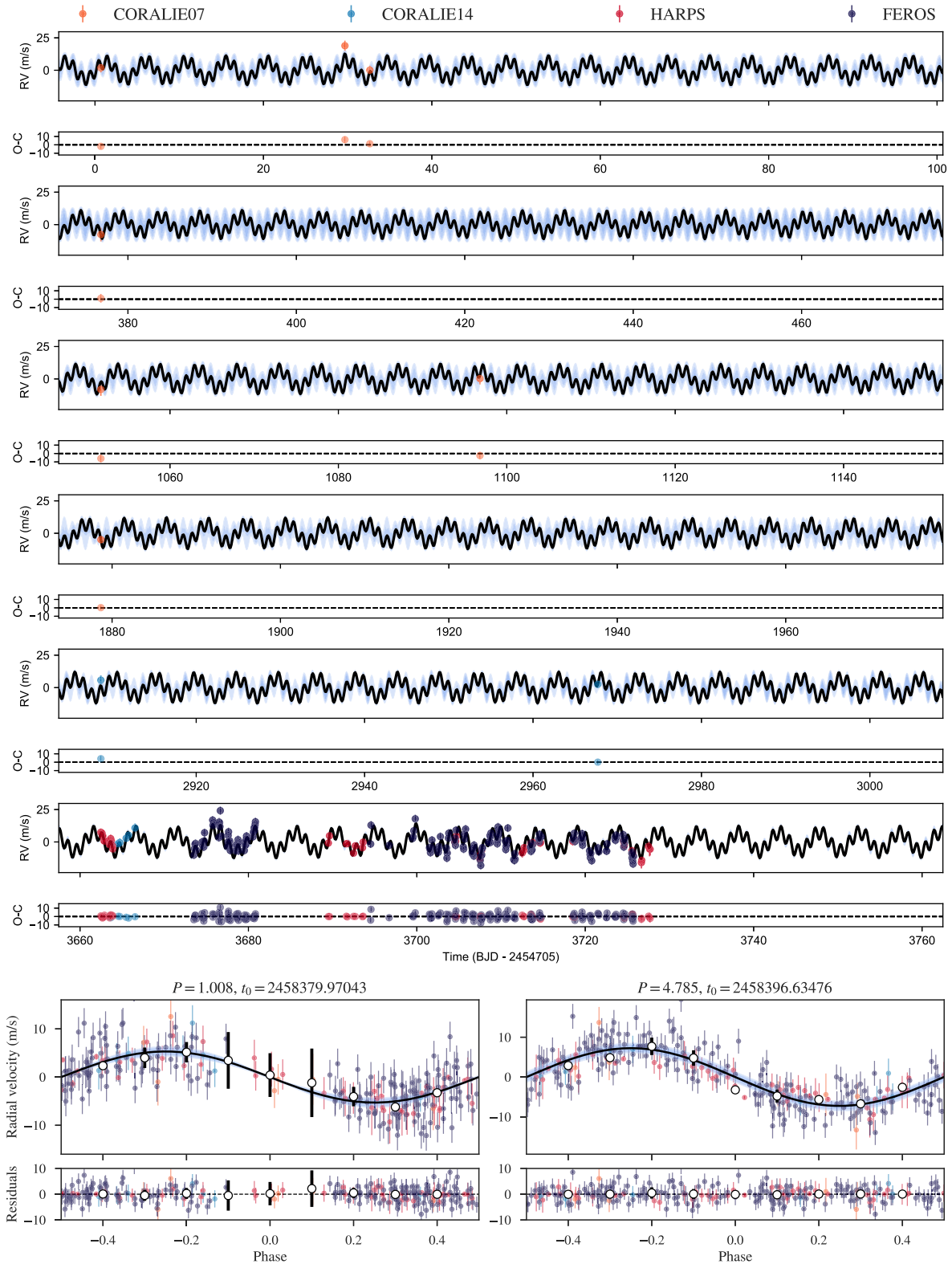
Figure 7. Systemic velocity-subtracted radial velocities for the TOI-141 system observed by our FEROS (dark blue), HARPS (red), and CORALIE (orange and light blue) observations. The top panel shows the radial velocities as a function of time along with the residuals (O–C) obtained from subtracting those with our median posterior model given the data (black lines; blue bands around it denoting 68 per cent, 95 per cent, and 99 per cent posterior credibility bands). Note the effects of the sampling of the inner, 1-d period planet, which made us sample almost identical phases on consecutive days. The bottom panel shows the phased radial velocities of TOI-141b (bottom left panel) and TOI-141c (bottom right panel) with the GP component removed, along with the phased residuals – white points show binned data points in phase for visualization. The same colouring as for the top panels is used for the bottom panels.
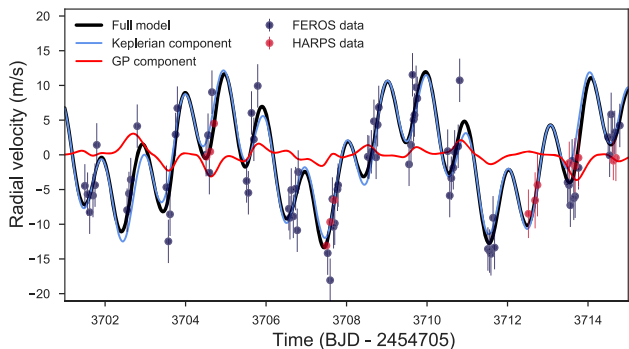
Figure 8. Close-up to the radial-velocity data set presented in Fig. 7, where we show each component of our best-fitting model (black line): the Keplerian (blue line) and the GP (red line) component.
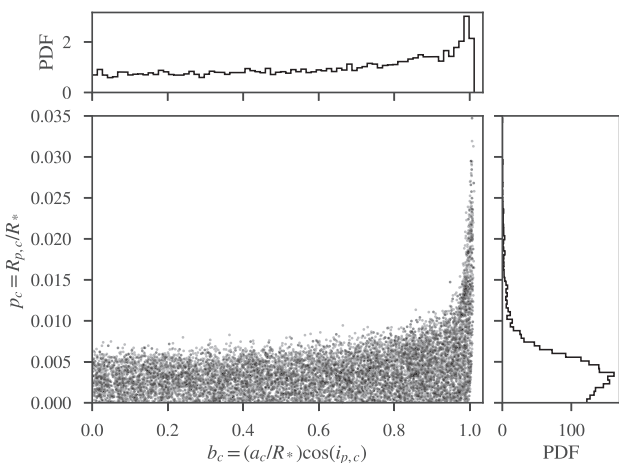
Figure 9. Posterior distribution of the impact parameter (b_c) and the planet-to-star radius ratio (p_c) for TOI-141c given the *TESS* photometry (central panel). The upper and right-hand panels show the marginal distributions of each of those parameters.

$b_c = (a_c/R_*)\cos(i_{p,c})$ (where a_c is the semimajor axis of planet c and $i_{p,c}$ is the inclination of planet c) and the planet-to-star radius ratio of the planet, $p_c = R_{p,c}/R_*$, in the case of the joint fit assuming TOI-141c transits. The marginal distribution of the planet-to-star radius ratio implies that even if the planet were to transit, about 95 per cent of the posterior density is bounded to be $p_c < 0.014$, i.e. a planetary radius $R_{p,c} < 1.7\,R_\oplus$. At the same time, in this transiting scenario the impact parameter, coupled with the tight constraint on the stellar density (and hence, on a_c/R_*) would imply that 95 per cent of the posterior density of the inclination is above $i_{p_c} > 84.82$, implying $\sin(i_{p_c}) > 0.996$, and hence making the true mass $19.95^{+1.38}_{-1.36}\,M_\oplus < M_p < 20.05^{+1.36}_{-1.39}\,M_\oplus$. This would in turn give rise to a density for TOI-141c about two times that of TOI-141b, which would imply an extremely dense object. The rareness of such an object thus adds to the statistical evidence that TOI-141c most likely does not transit TOI-141.

3.5 Secondary eclipses, phase-curve modulations, TTVs

A search for secondary eclipses and phase-curve modulations of either TOI-141b or TOI-141c turned out to be null in the *TESS* photometry. This is not surprising as both reflected and emitted light in the *TESS* bandpass for these exoplanets is expected to be
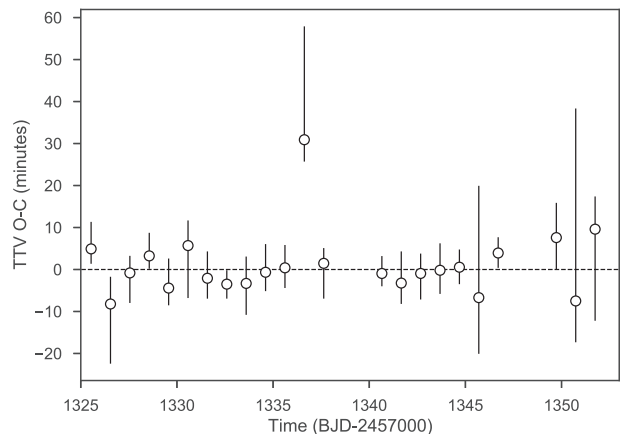
Figure 10. Transit timing variations (TTVs) for TOI-141b (i.e. observed minus expected time-of-transit centre as a function of time). No evident variation is observed, putting a limit of ∼2 min to any TTV for TOI-141b.

quite low; of the order of a couple of ppm for TOI-141b and a couple tens of ppm for TOI-141c depending on its size.

In addition, we performed a search for transit timing variations (TTVs) on the transits of TOI-141b. For this, we used the posterior transit parameters presented in Table 6 as priors for transit fits to the individual transits with JULIET where the time-of-transit centre was left as a free parameter with a uniform prior between 2 h before and 2 h after of the expected time of transit centre. The resulting measured TTVs are presented in Fig. 10. As can be seen, there are no evident TTVs, except for the 12th transit observed by *TESS*, which appears to be half an hour later than expected. However, inspecting this portion of the light curve there is an evident decrease of flux during egress, most likely arising from instrumental effects, which is what produces this significant shift in the time of transit. With our observations, we can put an upper limit of about 2 min over a course of 27 d to any TTVs impacting the time-of-transit centres of TOI-141b. This was expected at least for TTVs generated by TOI-141c on TOI-141b, for which an order-of-magnitude estimate gives a TTV amplitude of the order of 4 s (Holman & Murray 2005).

4 DISCUSSION

4.1 The TOI-141 system

The TOI-141 system composed of TOI-141b and TOI-141c is a very interesting system. On the one hand, TOI-141b, as will be shown below in Section 4.2, is a bona fide 'super-Earth', i.e. a rocky planet significantly larger than our home planet. Fig. 11 compares TOI-141b in particular in the mass–radius diagram of exoplanets smaller than 2 Earth-radii (retrieved from exoplanets.org) whose masses and radius are characterized at better than 20 per cent. We plot the two-layer models of Zeng et al. (2016) for illustration.

As can be seen from Fig. 11, TOI-141b appears to have a composition similar to that of the Earth according to two-layer models. In fact, among super-Earths, it appears this is one of the few exoplanets for which we can confidently claim this is the case, making it a very interesting exoplanet. This possibility will be discussed in detail in Section 4.2.

TOI-141c, on the other hand, is most likely a short-period Neptune if the mutual inclination with TOI-141b is not too large. We showed that given the data the most plausible scenario for TOI-141c is that it does not transit the star, and thus the maximum
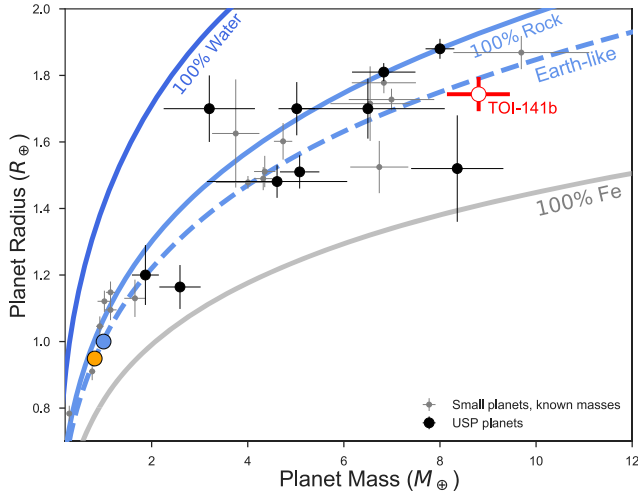
Figure 11. Mass–radius diagram for known exoplanets with sizes smaller than 2 Earth-radii. Black points identify USPs; TOI-141b is identified in red. Two-layer models are from Zeng, Sasselov & Jacobsen (2016); 'Earth-like' here means a composition of 30 per cent Fe and 70 per cent $MgSiO_3$, whereas '100 per cent Rock' means a composition of 100 per cent $MgSiO_3$. Earth is identified in this plot as a pale blue circle; the orange circle is Venus.

inclination of this planet with respect of the plane of the sky would be of $i_c < \arccos(a/R_*)^{-1}$, or $i_c < 84.829 \pm 0.051$ deg. This in turn implies that the true mass of TOI-141c is most likely $M_{p,c} > 18.54 \pm 0.85\,M_\oplus$. We are not able to put any constraints on the mutual inclination between TOI-141b and TOI-141c other than this upper limit for TOI-141c.

4.2 Interior composition of TOI-141b

4.2.1 Interior characterization: method

For a detailed interior characterization, we use the probabilistic analysis of Dorn et al. (2017) which calculates possible interiors given the observed data (e.g. mass and radius as shown in Fig. 11). Besides the data of mass and radius, we are using constraints on the possible bulk composition in terms of refractory elements (e.g. Fe, Mg, Si), which helps to refine interior predictions (Dorn et al. 2015). A proxy for the planet bulk composition is usually taken from the host star's photosphere. Here, measured stellar abundances of TOI-141b are (see Section 3.2) [Fe/H] $=-0.04 \pm 0.03$, [Mg/H] $=-0.04 \pm 0.06$, and [Si/H] $=-0.03 \pm 0.09$. Thus, relative stellar abundances of Fe/Si and Mg/Si are similar to the Sun. In brief, our data comprise:

(i) Planet masses and radii (Table 6).
(ii) Planet effective temperature (Table 6).
(iii) Relative stellar abundances of Fe, Si, and Mg of the host star.

Our assumptions for the interior model are similar to those in Dorn et al. (2017), but we consider a purely rocky planet. We assume an iron core and a silicate mantle, thus $r_{core + mantle}$ equals R_p. The interior parameters are core size r_{core} and mantle composition (i.e. Fe/Si$_{mantle}$, Mg/Si$_{mantle}$). The prior distributions of the interior parameters are stated in Table 7.

Our interior model uses a self-consistent thermodynamic model from Dorn et al. (2017). For any given set of interior parameters, it allows us to calculate the respective mass, radius, and bulk abundances and compare them to the actual observed data. The

Table 7. Prior ranges for interior parameters.

Parameter	Prior range	Distribution
Core radius r_{core}	$(0.01-1)\,r_{core + mantle}$	Uniform in r_{core}^3
Fe/Si$_{mantle}$	$0 - Fe/Si_{star}$	Uniform
Mg/Si$_{mantle}$	Mg/Si$_{star}$	Gaussian
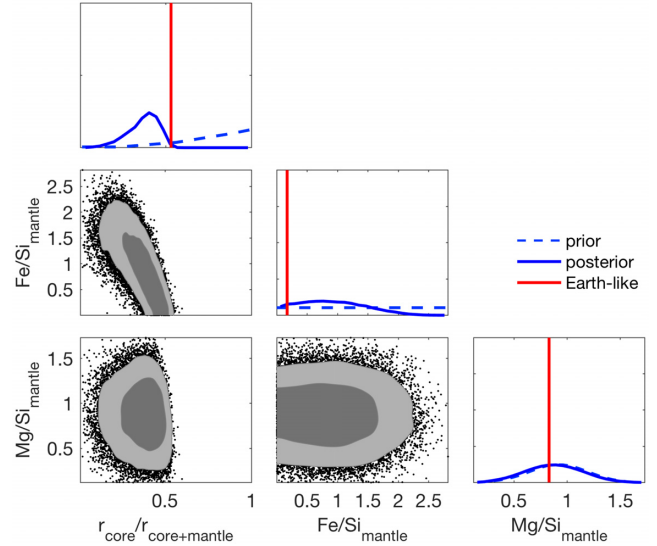
Figure 12. Two- and one-dimensional marginalized posteriors of interior parameters: core size (r_{core}) and mantle composition (Fe/Si$_{mantle}$ and Mg/Si$_{mantle}$). The prior distribution is shown in dashed, while the posterior distribution is shown in solid lines. An Earth-like interior is shown for reference.

Table 8. Interior parameter estimates. 1σ uncertainties of the 1D marginalized posteriors are listed.

Interior parameter	All constraints	No Fe/Si constraint	Earth-like value
$r_{core}/r_{core + mantle}$	$0.38^{+0.07}_{-0.11}$	$0.41^{+0.10}_{-0.12}$	0.53
Fe/Si$_{mantle}$	$0.87^{+0.60}_{-0.54}$	$1.51^{+1.46}_{-0.98}$	0.17
Mg/Si$_{mantle}$	$0.87^{+0.26}_{-0.25}$	$0.91^{+0.25}_{-0.25}$	0.83
$\rho_p/\rho_\oplus$	$1.53^{+0.07}_{-0.06}$	$1.67^{+0.13}_{-0.12}$	1.

thermodynamic model comprises the equation of state (EoS) of iron by Bouchet et al. (2013), the silicate-mantle model by Connolly (2009) to compute equilibrium mineralogy and density profiles given the data base of Stixrude & Lithgow-Bertelloni (2011). We assume an adiabatic temperature profile within core and mantle.

4.2.2 Interior characterization: results and discussion

Fig. 12 and Table 8 summarize posterior distributions of inferred interior parameters. Given bulk density, the planet is dominated by its rocky interior and might host a very thin terrestrial-type atmosphere only. The data of mass, radius, and bulk abundances inform possible core sizes and mantle compositions. Interestingly, the bulk abundance constraints cannot be reconciled with the measured bulk density of $\rho_p = 1.66\,\rho_\oplus$. This is because the abundance constraint favours Earth-like densities, while TOI-141b's bulk density is higher (see Fig. 11). In order to better fit the bulk density, we relaxed the constraint on Fe/Si in a separate scenario and thereby allowed for rocky interiors with larger core mass fractions

(Table 8). Although this scenario can well fit mass and radius, it remains unclear how such iron-rich interiors for massive super-Earths can be formed. The result of a possible iron-rich interior has to be discussed in light of our model assumptions and model uncertainties. Here, we have assumed pure iron cores for simplicity. The addition of light elements (e.g. O, Si, S, C) in the core can allow for larger cores and thus higher bulk densities, while fitting the measured bulk density. This suggests that the amount of light elements in the core can be constrained by mass, radius, and bulk abundances. Further investigations are underway to understand the importance of light core elements for super-Earths.

Here, we have chosen a rocky interior a priori and excluded atmospheres to significantly contribute to the planetary radius. We included possible terrestrial-like atmospheres in test runs that showed that possible atmosphere thicknesses are only tiny (0.01 R_p). Such thin atmospheres cannot be of primordial H/He, since atmospheric escape can efficiently erode thin H/He layer on short time-scales. An atmosphere of H/He is only stable against evaporative loss if it would be significantly thicker than the theoretical minimum threshold thickness (Dorn & Heng 2018), which is 0.18 R_p for TOI-141b. The threshold thickness corresponds to the amount of gas (H₂) that is lost on short time-scale (here we use 100 Myr).

If this planet has indeed an atmosphere that can be characterized by spectroscopy, this planet would be an interesting target for investigating whether the atmosphere's origin can be informed by the chemical make-up and the extent of the atmosphere. Terrestrial-type atmospheres can be built during the outgassing of a cooling magma ocean or by volcanism during the long-term evolution of a planet. The rate of volcanism can be very different depending on the convection regime of a planet, e.g. stagnant-lid versus plate tectonics (Kite, Manga & Gaidos 2009). If TOI-141b is in stagnant-lid regime, no massive terrestrial-like atmosphere is expected since outgassing rates are very limited for ≳8 M⊕ planets (Dorn, Noack & Rozel 2018) despite its partly unconstrained interior structure and composition. A massive atmosphere of volcanic origin could only be present if the planet is in a different convection than stagnant-lid, e.g. plate tectonics. From the variety of modelling studies (Valencia, O'connell & Sasselov 2007; Kite et al. 2009; Korenaga 2010; van Heck & Tackley 2011; Noack & Breuer 2014), however, it remains unclear whether super-Earths can drive plate tectonics or not.

4.3 Atmospheric characterization of TOI-141b

Along with Kepler-10b (Batalha et al. 2011), Kepler-78b (Sanchis-Ojeda et al. 2013), K2-141b (Malavolta et al. 2018), and 55 Cancri e, TOI-141b joins the select group of rocky exoplanets that might be optimal targets for further atmospheric characterization with current and upcoming facilities. Given TOI-141b is so similar to 55 Cancri e, an exoplanet that has received particular attention in this front in recent years (see e.g. Demory et al. 2016; Tsiaras et al. 2016; Angelo & Hu 2017; Miguel 2019), it is important to briefly discuss the prospects for atmospheric characterization of this newly discovered exoplanet. Among all the USPs, TOI-141b is the brightest one after 55 Cancri e. However, it is 2.4 mag fainter in K_s band and 2 mag fainter in V band than the latter. As such, this implies that characterizing the atmosphere of TOI-141b will be more challenging than the one performed so far for 55 Cancri e with known space telescopes such as *Spitzer* and *Hubble*. However, the fact that this provides one of the first exoplanets to perform a direct comparison to the observational properties of 55 Cancri e, makes this challenge a particularly interesting one to take. For the detection of the thermal emission for TOI-141b with *Spitzer*,

this might involve over 10 transits to detect an occultation at 3σ confidence. As for transmission, the fainter nature of TOI-141b might actually help if observations are to be carried out with *Hubble*. For 55 Cancri e, spatial scans which left larger trails than usual were used in order to compute a transmission spectrum with *HST*/WFC3 (see discussion in Tsiaras et al. 2016). It is possible that this led to precisions 5–20 per cent larger than the photon noise, whereas it is known that *Hubble* observations can achieve precisions close to 5 per cent the photon noise for bright stars (Knutson et al. 2014) – and thus this precision could be achieved for TOI-141b with *Hubble*. As such, TOI-141b might be an excellent target for transmission spectroscopy observations with current observatories.

For future *JWST* observations, the brightness of TOI-141 might impact on the type of observations that can be made *because the star is too bright*. However, observations with different instruments and filters might allow to characterize this exoplanet, especially at wavelengths >2 μm. For example, a wide range of *NIRCam* observations are possible to make for TOI-141b with a range of filters, which implies the thermal emission of this exoplanet might be easily detected with just one *JWST* transit. For transmission, *NIRISS* + *SOSS* observations will be possible for wavelengths ≳1.5 μm where the instrument saturation falls for magnitudes brighter than $J \sim 7$, allowing to target a wide range of possible molecular features for this exoplanet. In summary, thus, TOI-141b could be a prime target for *JWST* transit and occultation observations of hot super-Earths.

5 CONCLUSIONS

In this work, we have presented TOI-141b, a hot super-Earth orbiting in a 1-d period around the G-type star HD 213885 – the second brightest star known to host a USP exoplanet. The exoplanet was detected by *TESS* photometry and later confirmed and further characterized using precise RV observations with the CORALIE, HARPS, and FEROS spectrographs. Our observations reveal that TOI-141b has a rocky bulk composition, converting this exoplanet into a bona fide super-Earth: a rocky planet with a bulk composition similar (although enhanced in iron) to Earth. In addition, our precise radial-velocity measurements reveal the presence of an additional Neptune-mass exoplanet, TOI-141c, on a 4.78-d orbit which does not show transits in the *TESS* photometry.

TOI-141b is an interesting exoplanet from the perspective of atmospheric characterization of hot super-Earths and especially to be compared with 55 Cancri e, for which TOI-141b is a very similar exoplanet. Characterization of this exoplanet with both present (e.g. *HST*, *Spitzer*) and future (e.g. *JWST*) space-based facilities might help unveil the nature of the atmospheres of these kind of exoplanets, allowing to kickstart comparative exoplanetology of hot super-Earths.

REFERENCES

Ambikasaran S., Foreman-Mackey D., Greengard L., Hogg D. W., O'Neil M., 2016, IEEE Trans. Pattern Anal. Mach. Intell., 38, 252

Angelo I., Hu R., 2017, AJ, 154, 232

Baranne A., Mayor M., Poncet J. L., 1979, Vistas Astron., 23, 279

Batalha N. M. et al., 2011, ApJ, 729, 27

Bouchet J., Mazevet S., Morard G., Guyot F., Musella R., 2013, Phys. Rev. B, 87, 094102

Bourrier V. et al., 2018, A&A, 619, A1

Brahm R., Jordán A., Espinoza N., 2017a, PASP, 129, 034002

Brahm R., Jordán A., Hartman J., Bakos G., 2017b, MNRAS, 467, 971

Brahm R. et al., 2018a, MNRAS, 483, 1970

Brahm R. et al., 2018b, MNRAS, 477, 2572

Buchner J. et al., 2014, A&A, 564, A125

Carrier F., Bourban G., 2003, A&A, 406, L23

Castelli F., Kurucz R. L., 2003, in Piskunov N., Weiss W. W., Gray D. F., eds, Proc. IAU Symp. 210, Modelling of Stellar Atmospheres. Kluwer, Dordrecht, p. A20

Collins K. A., Kielkopf J. F., Stassun K. G., Hessman F. V., 2017, AJ, 153, 77

Connolly J., 2009, Geochem., Geophys., Geosyst., 10

Dai F., Masuda K., Winn J. N., 2018, ApJ, 864, L38

Dawson R. I., Fabrycky D. C., 2010, ApJ, 722, 937

Delgado Mena E., Israelian G., González Hernández J. I., Bond J. C., Santos N. C., Udry S., Mayor M., 2010, ApJ, 725, 2349

Demory B.-O. et al., 2016, Nature, 532, 207

Dorn C., Heng K., 2018, ApJ, 853, 64

Dorn C., Khan A., Heng K., Connolly J. A. D., Alibert Y., Benz W., Tackley P., 2015, A&A, 577, A83

Dorn C., Venturini J., Khan A., Heng K., Alibert Y., Helled R., Rivoldini A., Benz W., 2017, A&A, 597, 37

Dorn C., Noack L., Rozel A. B., 2018, A&A, 614, A18

Elsworth Y. P., Thompson M. J., 2004, Astron. Geophys., 45, 5.14

Espinoza N., 2018, Res. Notes Am. Astron. Soc., 2, 209

Espinoza N., Kossakowski D., Brahm R., 2019, MNRAS, 490, 2262

Feroz F., Hobson M. P., Bridges M., 2009, MNRAS, 398, 1601

Fischer D. A. et al., 2008, ApJ, 675, 790

Foreman-Mackey D., Agol E., Ambikasaran S., Angus R., 2017, AJ, 154, 220

Fulton B. J., Petigura E. A., Blunt S., Sinukoff E., 2018, PASP, 130, 044504

Gaia Collaboration, 2018, A&A, 616, A1

Henry T. J., Soderblom D. R., Donahue R. A., Baliunas S. L., 1996, AJ, 111, 439

Holman M. J., Murray N. W., 2005, Science, 307, 1288

Huang C. X. et al., 2018, ApJ, 868, L39

Jenkins J. M. et al., 2016, in Chiozzi G., Guzman J. C., eds, Proc. SPIE Conf. Ser. Vol. 9913, Software and Cyberinfrastructure for Astronomy IV. SPIE, Bellingham, p. 99133E

Jensen E., 2013, Astrophysics Source Code Library, record ascl:1306.007

Kaufer A., Pasquini L., 1998, in D'Odorico S., ed., Proc. SPIE Conf. Ser. Vol. 3355, Optical Astronomical Instrumentation. SPIE, Bellingham, p. 844

Kipping D. M., 2013, MNRAS, 435, 2152

Kite E. S., Manga M., Gaidos E., 2009, ApJ, 700, 1732

Knutson H. A. et al., 2014, ApJ, 794, 155

Korenaga J., 2010, ApJ, 725, L43

Kovács G., Zucker S., Mazeh T., 2002, A&A, 391, 369

Kreidberg L., 2015, PASP, 127, 1161

Li J., Tenenbaum P., Twicken J. D., Burke C. J., Jenkins J. M., Quintana E. V., Rowe J. F., Seader S. E., 2019, PASP, 131, 024506

Malavolta L. et al., 2018, AJ, 155, 107

Maxted P. F. L. et al., 2016, A&A, 591, A55

Mayor M. et al., 2003, Messenger, 114, 20

Miguel Y., 2019, MNRAS, 482, 2893

Nelson B. E., Ford E. B., Buchner J., Cloutier R., Díaz R. F., Faria J. P., Rajpaul V. M., Rukdee S., 2018, preprint (arXiv:1806.04683)

Neves V., Santos N. C., Sousa S. G., Correia A. C. M., Israelian G., 2009, A&A, 497, 563

Noack L., Breuer D., 2014, Planet. Space Sci., 98, 41

Petrovich C., Deibert E., Wu Y., 2019, AJ, 157, 180

Queloz D. et al., 2001, Messenger, 105, 1

Ricker G. R. et al., 2015, J. Astron. Telesc. Instrum. Syst., 1, 014003

Sanchis-Ojeda R., Rappaport S., Winn J. N., Levine A., Kotson M. C., Latham D. W., Buchhave L. A., 2013, ApJ, 774, 54

Sanchis-Ojeda R., Rappaport S., Winn J. N., Kotson M. C., Levine A., El Mellah I., 2014, ApJ, 787, 47

Smith J. C. et al., 2012, PASP, 124, 1000

Sneden C., 1973, ApJ, 184, 839

Stassun K. G. et al., 2018, AJ, 156, 102

Stixrude L., Lithgow-Bertelloni C., 2011, Geophys. J. Int., 184, 1180

Stumpe M. C. et al., 2012, PASP, 124, 985

Stumpe M. C., Smith J. C., Catanzarite J. H., Van Cleve J. E., Jenkins J. M., Twicken J. D., Girouard F. R., 2014, PASP, 126, 100

Tokovinin A., 2018, PASP, 130, 035002

Tsiaras A. et al., 2016, ApJ, 820, 99

Twicken J. D. et al., 2018, PASP, 130, 064502

Valencia D., O'connell R. J., Sasselov D. D., 2007, ApJ, 670, L45

Vanderplas J., Connolly A., Ivezić Ž., Gray A., 2012, Conference on Intelligent Data Understanding (CIDU), IEEE. p. 47

van Heck H. J., Tackley P. J., 2011, Earth Planet. Sci. Lett., 310, 252

Winn J. N. et al., 2011, ApJ, 737, L18

Winn J. N., Sanchis-Ojeda R., Rappaport S., 2018, New Astron. Rev., 83, 37

Yi S., Demarque P., Kim Y.-C., Lee Y.-W., Ree C. H., Lejeune T., Barnes S., 2001, ApJS, 136, 417

Zechmeister M., Kürster M., 2009, A&A, 496, 577

Zeng L., Sasselov D. D., Jacobsen S. B., 2016, ApJ, 819, 127

SUPPORTING INFORMATION

Supplementary data are available at *MNRAS* online.

Table 1. Radial-velocity measurements obtained for TOI-141.

Please note: Oxford University Press is not responsible for the content or functionality of any supporting materials supplied by the authors. Any queries (other than missing material) should be directed to the corresponding author for the article.

[1] *Space Telescope Science Institute, 3700 San Martin Drive, Baltimore, MD 21218, USA*

[2] *Max-Planck-Institut für Astronomie, Königstuhl 17, D-69117 Heidelberg, Germany*

[3] *Center of Astro-Engineering UC, Pontificia Universidad Católica de Chile, 7820436 Santiago, Chile*

[4] *Instituto de Astrofísica, Facultad de Física, Pontificia Universidad Católica de Chile, 7820436 Santiago, Chile*

[5] *Millennium Institute for Astrophysics, 7820436 Santiago, Chile*

[6] *Facultad de Ingeniería y Ciencias, Universidad Adolfo Ibáñez, Av. Diagonal las Torres 2640, Peñalolén, 7941169 Santiago, Chile*

[7] *Instituto de Astrofísica, Facultad de Fisica, Pontificia Universidad Catolica de Chile, Av. Vicuña Mackenna 4860, 782-0436 Macul, Santiago, Chile*

[8] *University of Zurich, Institut of Computational Sciences, University of Zurich, Winterthurerstrasse 190, CH-8057 Zurich, Switzerland*

[9] *Departamento de Astronomía, Universidad de Chile, Camino El Observatorio 1515, Las Condes, Santiago, Chile*

[10] *Departamento de Ciencias Físicas, Facultad de Ciencias Exactas, Universidad Andrés Bello, Las Condes, RM, Santiago, Chile*

[11] *NASA Ames Research Center, Moffett Field, CA 94035, USA*

[12] *SETI Institute, Moffett Field, CA 94035, USA*

[13] *Center for Astrophysics | Harvard & Smithsonian, 60 Garden Street, Cambridge, MA 02138, USA*

[14] *Department of Physics, University of Warwick, Gibbet Hill Road, Coventry CV4 7AL, UK*

[15] *Centre for Exoplanets and Habitability, University of Warwick, Gibbet Hill Road, Coventry CV4 7AL, UK*

[16] *Instituto de Astrofísica e Ciências do Espaço, Universidade do Porto, CAUP, Rua das Estrelas, P-4150-762 Porto, Portugal*

[17] *Depto. Astrofúisica, Centro de Astrobiología (CSIC-INTA), ESAC campus, Camino Bajo del Castillo s/n, E-28692 Villanueva de la Cañada Madrid, Spain*

[18] *Observatoire de l'Université de Genève, 51 chemin des Maillettes, CH-1290 Versoix, Switzerland*

[19] *European Southern Observatory, Alonso de Cordova 3107, Vitacura Casilla 19001, Santiago 19, Chile*

[20] *Departamento de Física e Astronomia, Faculdade de Ciências, Universidade do Porto, Rua do Campo Alegre, P-4169-007 Porto, Portugal*

[21] *Department of Physics and Kavli Institute for Astrophysics and Space Science, Massachusetts Institute of Technology, Cambridge, MA 02139, USA*

[22] *Department of Astrophysical Sciences, Princeton University, Princeton, NJ 08544, USA*

[23] *Department of Physics and Astronomy, University of Louisville, Louisville, KY 40292, USA*

[24] *Computational Engineering and Science Research Centre, University of Southern Queensland, Toowoomba, QLD 4350, Australia*

[25] *Mt. Stuart Observatory, New Zealand*

[26] *Department of Physics & Astronomy, Swarthmore College, Swarthmore, PA 19081, USA*

[27] *Nicolaus Copernicus Astronomical Center, Polish Academy of Sciences, ul. Rabiańska 8, PL-87-100 Toruń, Poland*

[28] *Cerro Tololo Inter-American Observatory, National Optical Astronomical Observatory, Casilla 603, La Serena 1700000, Chile*

[29] *Dunlap Institute for Astronomy and Astrophysics, University of Toronto, Ontario M5S 3H4, Canada*

[30] *Department of Physics and Astronomy, University of North Carolina at Chapel Hill, Chapel Hill, NC 27599-3255, USA*

[31] *Noqsi Aerospace Ltd, 15 Blanchard Ave., Billerica, MA 01821, USA*

[32] *Exoplanets and Stellar Astrophysics Laboratory, Code 667, NASA Goddard Space Flight Center, Greenbelt, MD 20771, USA*

[33] *Millenium Engineering and Integration, Co., 1400 Crystal Dr 800, Arlington, VA 22202, USA*

This paper has been typeset from a TEX/LATEX file prepared by the author.